Research Square

Preprints are preliminary reports that have not undergone peer review.
They should not be considered conclusive, used to inform clinical practice,
or referenced by the media as validated information.

Overcoming conventional trade-offs in strain sensing with physics-guided inverse design of aperiodic architected nanocomposites

Francisco Molina-Lopez

francisco.molinalopez@kuleuven.be

KU Leuven

Viktor Naenen

KU Leuven

Stijn De Smedt

KU Leuven

Altynay Kaidarova

KU Leuven

Ruth Cardinaels

KU Leuven

Article

Keywords:

Posted Date: October 22nd, 2026

DOI: https://doi.org/10.21203/rs.3.rs-10804825/v1

License: This work is licensed under a Creative Commons Attribution 4.0 International License.
Read Full License

Additional Declarations: There is **NO** Competing Interest.

Overcoming conventional trade-offs in strain sensing with physics-guided inverse design of aperiodic architected nanocomposites

V. Naenen, S. De Smedt, A. Kaidarova, R. Cardinaels, F. Molina-Lopez
Department of Materials Engineering, KU Leuven, Kasteelpark Arenberg 44, 3001, Leuven, Belgium.

E-mail: francisco.molinalopez@kuleuven.be

Funding. V. N. is supported by FWO Research Foundation – Flanders, project 11K9223N. A.K. is supported by Research Foundation – Flanders (FWO) under grant no. 1228525N. S. De Smedt and R. Cardinaels are supported by the European Research Council (ERC) under the European Union's Horizon 2020 research and innovation programme: Grant Agreement No. 948739 – PEM-Sprint.

Keywords: physics-guided sensor design; electromechanical metamaterials; piezoresistive strain sensors; nanocomposites; direct ink writing; concentration-graded composites

Abstract

Large-strain piezoresistive sensors are critical for wearables and soft robotics. Still, conventional hyperelastic materials suffer from a trade-off between sensitivity, linearity, and strain range due to their intrinsic nonlinear electromechanical response. Here, we introduce a new class of aperiodic electromechanical metamaterials, where spatially graded carbon nanotube (CNT)-polydimethylsiloxane (PDMS) composites are architected into hierarchical networks via direct ink writing (DIW) of adjacent cells with varying filler concentrations. The resulting interdependence among cells gives rise to emergent electromechanical responses that are governed by architectural organization rather than intrinsic material properties, unlocking combinations of sensitivity, linearity, and strain range inaccessible to homogeneous composites and thereby expanding the accessible performance space. A physics-guided framework maps how local cell behavior propagates through the hierarchy, enabling rational inverse design through systematic exploration of this expanded performance space toward targeted electromechanical functionality. This transforms sensor development from costly trial-and-error optimization and data-intensive black-box AI models into an interpretable, physics-guided design process. Experimental validation confirmed metamaterials-based piezoresistors exhibiting a fourfold enhanced sensitivity (gauge factor 1.55) compared to their most linear homogeneous constituent material, while preserving an extreme linearity ($R^2 > 0.98$) over a 30% strain range, and tenfold enhanced sensitivity (gauge factor 37.5) compared to the most sensitive constituent material. As proof of concept, these metamaterials served as strain gauges for accurate respiratory monitoring. Most importantly, this physics-guided universal framework introduces a rational inverse-design paradigm for hierarchical nanocomposites, in which tailored electromechanical responses arise from architectural organization rather than from intrinsic material properties, enabling navigation of the expanded performance space toward application-specific functionality. Grounded in fundamental physical interactions, it enables systematic, interpretable design and extends naturally to other electromechanical sensing modes, such as transverse piezoresistivity and piezocapacitance, for potential applications in multi-modal sensing, soft robotics, stretchable transistors, and adaptive structures.

1. Introduction

Large-strain sensors are essential in soft robotics, wearable electronics, and human–machine interfaces, where they must combine electrical conductance, mechanical robustness, and reversible large strains above the 1 % elastic limit of metals. To achieve this, elastomeric matrices are typically blended with conducting fillers to form percolative networks[1]. A central challenge in these hybrid composite sensors is the intrinsic trade-off between sensitivity, linearity, and strain range, arising from their nonlinear electromechanical response[1–5].

Sensitivity is characterized by the gauge factor (GF), measuring the relative resistance change ($\Delta R/R_0$) per unit of strain (ε). High sensitivity enables the resolution of small strain variations. Linearity, commonly quantified by the coefficient of determination, R^2, obtained from linear regression of the resistance-strain $R(\varepsilon)$ curve, is equally important: it enables reliable strain estimation with minimal signal processing, owing to straightforward calibration and undistorted noise, i.e., noise that preserves its statistical symmetry and does not introduce bias: Symmetric noise in the measured resistance (σ^2_{noise}) introduces a bias in the estimated strain of approx. $\frac{1}{2}\frac{d^2\varepsilon}{dR^2}\sigma^2_{noise}$, for nonlinear $R(\varepsilon)$ responses[6]. The usable strain range - the linear region of the $R(\varepsilon)$ curve - must be clearly distinguished from stretchability, a term often ambiguously used in the literature. Figure S1 illustrates the difference. From an electrical perspective, stretchability refers to the maximum strain where resistance remains measurable. From a mechanical perspective, stretchability may refer to the material fracture strain (or elongation at break), which can reach several hundred percent and is particularly relevant for stretchable interconnects and devices designed to withstand extreme deformations.

Percolated conducting nanocomposites inherently exhibit nonlinear electromechanical behavior as a result of strain continuously altering geometry, percolation pathways, and tunneling junction distances[2–4]. This nonlinearity arises from two mechanisms: geometric deformation, which produces a superlinear $R(\varepsilon)$ response $\sim(1+\varepsilon)^{1+2\nu}$ in bulk conductors according to Pouillet's law[7] (ν being the Poisson's ratio), and strain-dependent tunneling, which further amplifies nonlinearity through an exponential resistivity dependence $\sim e^{\beta(d-d_0)}$ (where d_0 and d are the initial and strained distance between fillers, and β is the tunneling decay constant)[3]. Together, these mechanisms yield a nonlinear, continuously accelerating $R(\varepsilon)$ curve (see SI2)[5]. The piezoresistive response is therefore often approximated by multiple locally linear intervals. Consequently, only the first linear interval permits a meaningful definition of the linear sensor metrics GF, R^2, and strain range.

Tuning the concentration of composites results in a predictable trade-off: fragile networks near the percolation threshold show high sensitivity to external disturbances such as strain, at the expense of stretchability[1,8–10]. Thus, recent efforts explored alternative architectures[5,10–12]: (i) internal structures such as self-separating filler clusters or porous structures for sensitivity; (ii) wrinkled or microcracked surface structures for reversible stretchability[13]; (iii) macroscopic structures, such as fibrous textiles, sandwiched sensing layers[14], or functionally separated sensing and interconnect composites[15]. SI3 provides a literature comparison of *GF*, R^2, and strain range. While these approaches enhance performance, they are specific to the material and architecture, and the relation between global sensor behavior and local material properties or device design is largely unexplored[16] – a gap this work addresses.

Recently, mechanical metamaterial strain sensors—primarily using auxetic substrates—have expanded the accessible piezoresistive performance space by reshaping deformation pathways, strain localization, and Poisson-ratio effects to tailor the response of a separately deposited conductive sensing layer. While highly effective, this substrate-centric approach relies on decoupled mechanical and sensing layers, where the electrical response of the sensing layer is passively dictated by the substrate's mechanical behavior, without interdependence[17–22].

In contrast, this work introduces two innovations: (i) Aperiodic metamaterials that integrate mechanical and sensing functions into a single, interdependent system. The structure is produced by direct ink writing (DIW) of spatially graded CNT-PDMS composites. Discrete cells with distinct filler concentrations form hierarchical networks by connecting in series to form branches, which are connected in parallel[23]. This architecture creates interdependence among cells due to strain redistribution, enabling the metamaterials to escape the conventional trade-offs between sensitivity, linearity, and strain range that constrain uniform composites, thereby expanding the accessible performance space. (ii) A physics-guided framework that maps how local cell behavior propagates through the hierarchical network to define global response, to navigate the expanded performance space created by the metamaterials. The framework employs an inverse design approach to identify architectures with targeted combinations of sensitivity, linearity, and strain range through prediction, rather than costly experimental trial-and-error or data-intensive black-box models. The framework is grounded in fundamental physical laws, including mechanical equilibrium (iso-stress for cells in series and iso-strain for branches in parallel) and equivalent-resistance calculations, making the framework interpretable and broadly applicable. It is material- and functionality-agnostic, applying to any hierarchical system where mechanical and functional properties interact.

The model is validated both mechanically (cell strain) and electrically (branch resistance) by comparing experiment with model estimate. Experimental validation confirmed its predictive power: metamaterials unlocked combinations of sensitivity, linearity, and strain inaccessible to uniform composites. Highly linear metamaterials ($R^2 > 0.98$) achieved a fourfold sensitivity increase over the most linear composite (0.82 vol% CNTs): *GF* 1.55 vs 0.39 up to a 30% strain range. For high-sensitivity sensing where linearity can be relaxed ($R^2 > 0.85$), the most sensitive composite (0.23 vol% CNTs) was outperformed by a factor of two (*GF* 7.11 vs 3.59 over a 50% strain range), or even by a factor of ten (*GF* 37.5 over a 38% strain range). In real-world testing, the metamaterials exhibited amplified sensitivity and/or linearity over their composite counterparts during on-body respiratory measurements. This new metamaterial not only unlocks extraordinary combinations of sensitivity, linearity, and strain range for piezoresistive strain sensing, but also represents a paradigm shift. The significance lies not in maximizing a single metric such as gauge factor, but in enabling access to and navigation of an expanded performance space. There is no universally optimal electromechanical material, because different applications require fundamentally different responses, ranging from highly sensitive strain sensors to strain-insensitive stretchable electronics such as transistors, amplifiers, and interconnects. By expanding and mapping the accessible performance space, the framework enables rational inverse design of architectures that maximize, minimize, or otherwise tailor functionality according to application-specific requirements, where the targeted responses emerge from structural organization rather than intrinsic material properties. This approach enables target-driven design across alternate sensing modes and applications, including multi-modal sensing, next-generation wearables, and soft robotics.

2. Results and Discussion

2.1. Direct Ink Writing of Concentration Tunable CNT/PDMS Nanocomposites

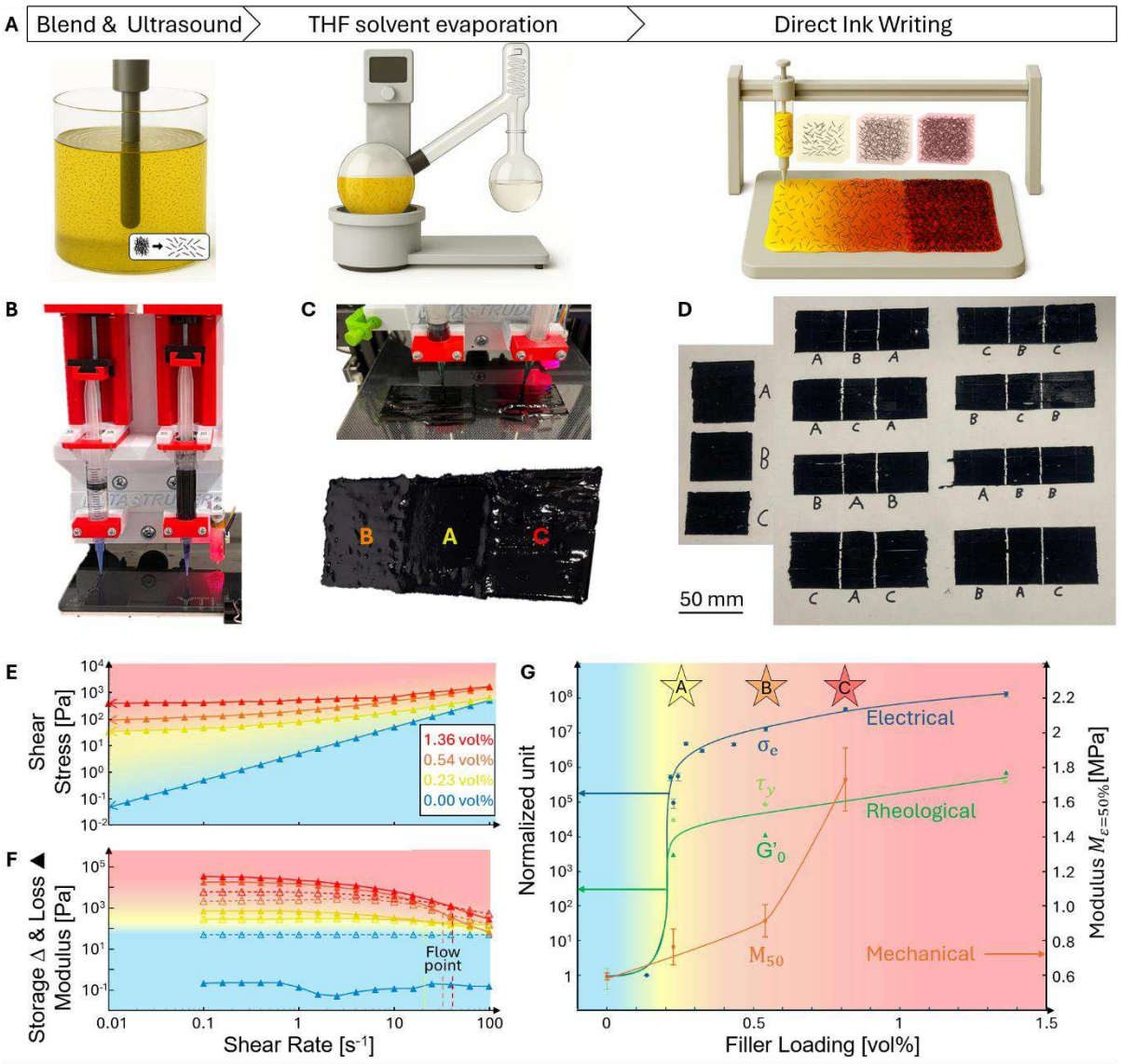

Figure 1. Fabrication and percolation behavior of concentration-graded CNT/PDMS composites. **(A)** Preparation of CNT/PDMS inks via ultrasonication, solvent removal, and direct ink writing (DIW), enabling spatially controlled deposition of graded concentrations within a printed branch. **(B, C)** Dual syringe DIW set-up to print branches with varying concentration. **(D)** Printed cells (left) and branches (right), with chalk markings indicating cell separation. **(E, F)** Rheology of CNT-PDMS inks: shear stress and storage/loss modulus vs shear rate. **(G)** Percolation behavior of CNT-PDMS inks (rheological) and solidified films (electrical conductivity σ_e and mechanical stiffness $M_{\varepsilon=50\%}$: Modulus at 50% strain), as a function of filler loading. The stars labeled A, B, and C indicate the filler loading of the three cell materials.

A platform enabling spatial control of CNT concentration was established to fabricate hierarchical architectures (Figure 1A), which is critical to achieve interdependent cells that produce emergent responses that cannot be replicated in uniform composites.

Composite inks were formulated by mixing elastomer (polydimethylsiloxane, PDMS) and fillers (CNTs) in a solvent (tetrahydrofuran, THF), followed by ultrasonication to enhance CNT dispersion, before solvent removal using a rotary evaporator. Spatially graded architectures were produced by direct ink writing (DIW) with an in-house developed multi-material DIW add-on for a commercial FDM printer[23]. For this purpose, inks with different CNT loadings were switched during printing to define cells with programmed composition and electrochemical behavior. The cells were then arranged in series into branches (Figure 1B-D).

The rheological response of PDMS–CNT inks with filler loading shows the emergence and strengthening of a percolated CNT network that increasingly governed flow and deformation. The shear-stress curves (Figure 1E) captured this transition directly: Contrary to uncured pure PDMS ink, all composite inks displayed the two-regime form of a Herschel–Bulkley fluid:

$$\tau = \tau_0 + k\dot{\gamma}^{\,n}, \qquad \text{(Eq. 1)}$$

For low shear rates $\dot{\gamma}$, there is a constant shear stress (τ_0, yield stress) where the CNT network resisted deformation t, followed by a flow regime at high shear rates $\dot{\gamma}$ where this network was overcome, and stress increased with shear rate (with the slope equal to the flow index n). k is the consistency index; more details are provided in SI4. Figure 1(E,G) shows that the yield stress (τ_0) rose strongly with CNT loading, reaching the DIW-suitable 10^2–10^3 Pa range required for shape retention and filament stability[24]. The flow index n (corresponding to the slope at high shear rates) decreased from ~1 (Newtonian fluid) for pure PDMS to ~0.55 (shear-thinning) for the composite inks. Beyond the yield stress, the network reorganized, giving rise to the strong shear-thinning required for DIW. Inks easily flowed during extrusion, while recovering solid-like integrity with high yield strength after deposition. Oscillatory measurements (Figure 1F) corroborated the network-dominated response: Pure PDMS behaved liquid-like with $G' < G''$ for the entire strain and frequency window tested, whereas CNT-filled inks at low frequencies and strains behaved as elastic solids with $G' > G''$, consistent with a percolated elastic network. The flow point (strain at the G'–G'' crossover) increased with CNT loading, similar to τ_0. The zero-frequency storage modulus G', which provides a measure of network stiffness, also increased with filler loading (Figure 1G).

The evolution of n, τ_0 and G'/G'' provides a coherent picture of the emergence and reinforcement of a CNT percolation network in the composite inks. These are suitable for DIW, combining shear-thinning, a finite yield stress, and elastic solid-like behavior at low shear strain and viscous flowing behavior at high shear strain. SI4 provides a detailed rheological analysis, including Herschel–Bulkley fits and DIW criteria.

After curing, the CNT/PDMS solid films demonstrated electrical percolation, where electrical conductivity (σ_e) abruptly increased when the filler loading (ϕ) reached a critical value (ϕ_c), known as the percolation threshold (Figure 1G-yellow). This behavior is described by[1]:

$$\sigma_{e,composite} = \sigma_{e,filler}(\phi - \phi_c)^t, \quad \text{(Eq. 2)}$$

with ϕ_c = 0.18 vol%. $\sigma_{e,composite}$ and $\sigma_{e,filler}$ are the electrical conductivities of the composite and filler. The low ϕ_c reflects efficient network formation characteristic of high-aspect-ratio CNTs, while the high percolation exponent (t = 2.97) suggests tunneling-dominated transport and microstructural heterogeneity[1]. Conductivity plateaued around 10^{-4} S·cm^{-1} at high loading (Figure S4). Three CNT concentrations near-above ϕ_c were selected for the cell constituent materials to span a wide range of electromechanical behavior, enabling strain redistribution and interdependence when combined in the metamaterial. The three materials are represented by star markers in Figure 1G: 0.23 vol% (A, yellow); 0.55 vol% (B, orange); 0.82 vol% (C, red).

The tensile modulus at 50% strain (M_{50}) shows a subtle, near-linear stiffening of the composites with CNT loading, increasing from 0.57 MPa (PDMS) up to 1.54 MPa (0.82 vol%, Figure 1G). A subtle percolation-like rise emerges at the upper end, yet the overall mechanical evolution remains far more limited than the pronounced electrical percolation transition.

2.2. Physics-based hierarchical framework

Analytical electromechanical models can predict sensor responses by coupling deformation models with equivalent circuit representation[25]. Figure 2 summarizes the physics-based model used to design metamaterial piezoresistive strain gauges with predictable behavior beyond that of the homogeneous constituent materials. SI6 provides a detailed description of the model. A cell is a region made of a traditional composite material with a fixed loading of CNTs uniformly dispersed into PDMS (called constituent materials). The electromechanical response of the constituent materials was characterized via synchronized tensile and resistance measurements, yielding constitutive relations for mechanical $\sigma(\varepsilon)$ and electrical $R(\varepsilon)$ behavior, shown in Figure 2 (panel 1. Cell, more info in SI6.1). Cells connect in series to form branches (panel 2. Branch), and branches connect in parallel to form a network (panel 3. Network), defining the target metamaterial. The figure maps how the behavior of the constituent materials (A,B,C) propagates through the hierarchy of cells → branches → network (more info in SI6.2). The framework therefore provides not only predictive capability, but also mechanistic insight by tracing how local cell behavior gives rise to the emergent network response. Because the hierarchical design method operates on experimentally determined constitutive relations and governing physical laws, it is not restricted to the CNT/PDMS material demonstrated here.

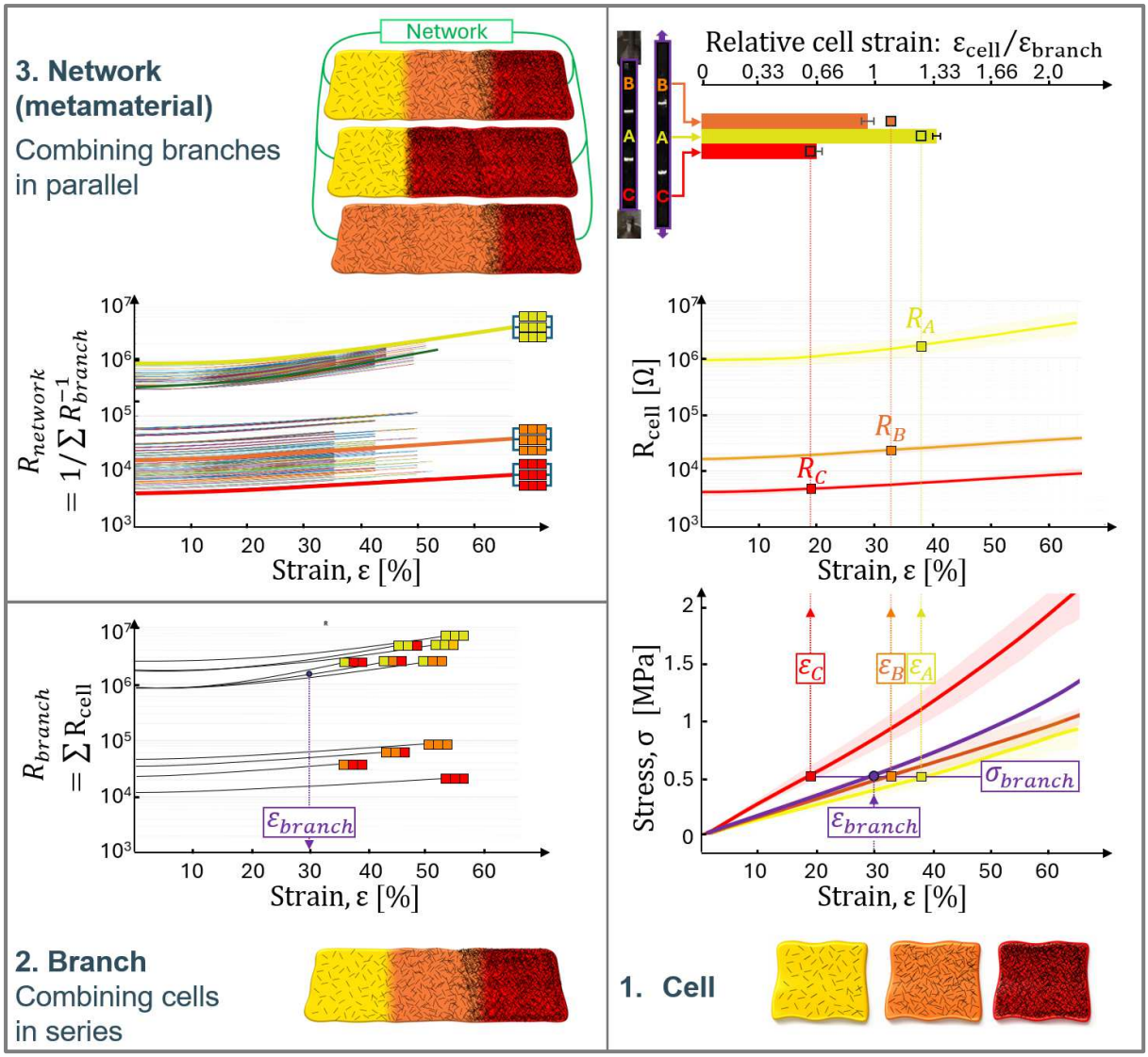

Figure 2. Physics-based model predicting how behavior propagates through the hierarchical network. The architecture of a given $R(\varepsilon)$ curve is indicated by its cells (A: yellow, B: orange, C: red). **(3) Network:** branches connected in parallel satisfy iso-strain conditions, yielding the network response through parallel resistance combination. **(2) Branch:** cells connected in series satisfy iso-stress conditions, and the branch resistance is obtained through series addition of the cell resistances. **(1) Cell:** The applied branch ε_{branch} strain leads to strain redistribution in the cells, where local cell strains ($\varepsilon_{A,B,C}$) vary to determine cell resistances ($R_{A,B,C}$). Experimentally measured $\sigma(\varepsilon)$ and $R(\varepsilon)$ relations serve as constitutive input curves. The relative cell strain bars are experimental observations (error bar is standard error) that are compared to their theoretical estimates (squares).

Since each network in panel 3 combines branches in parallel, the network resistance is $R_{network}(\varepsilon_{\text{network}}) = 1/\sum_{\text{branch}} R_{\text{branch}}^{-1}(\varepsilon_{\text{branch}})$. Note that branches experience the global strain ($\varepsilon_{\text{network}} = \varepsilon_{\text{branch}}$, iso-strain condition). Each branch in panel 2 consists of cells in series, hence $R_{\text{branch}}(\varepsilon_{\text{branch}}) = \sum_{cell} R_{\text{cell}}(\varepsilon_{\text{cell}})$. Here, each R_{cell} is obtained by inserting the cell strain $\varepsilon_{\text{cell}}$ into its experimental piezoresistive constitutive $R(\varepsilon)$ curve (panel 1). Thus, knowing the network response requires predicting the local cell strains.

All cells in a branch experience the same stress σ_{branch} (iso-stress condition), which translates into a certain branch strain $\varepsilon_{\text{branch}}$. Since each cell has a different stiffness, each cell will undergo a different strain (panel 1). The top bar in panel 1 illustrates the strain-redistribution mechanism by the relative cell strains, $\varepsilon_{\text{cell}}/\varepsilon_{\text{branch}}$ in a representative ABC branch, by comparing model predictions (squares) with image-based strain measurements (bars, more info on this method in SI6.2.2 and video SI1). Full validation across all branches is provided in Figure S9. Across all branch configurations, we observe that: (i) softer materials deform more ($\varepsilon_A > \varepsilon_B > \varepsilon_C$); (ii) the model succeeds in approximating experimental cell strains; and (iii) the relative cell strain depends on the branch configuration. For example, an A-cell deforms more in an ACC branch than in an AAA branch. This architecture-dependent redistribution means that the cells are interdependent, where device behavior emerges from interactions between constituent materials, opening a large design space that breaks the conventional averaging behavior of homogeneous composites and enables performance combinations beyond the trade-offs imposed by constituent materials. Importantly, the resulting electromechanical response can be traced directly to the strain-redistribution mechanism.

The device response depends only on the amount of each constituent material within a branch and the amount of each branch configuration within a network, not on their spatial order. Thus, the number of unique branch and network configurations follows a combinations-with-repetition counting (SI6.2.4). The number of possible branches composed of N_c cells made from N_m constituent materials is the binomial coefficient: $N_b = \binom{N_c+N_m-1}{N_c} = \frac{(N_c+N_m-1)!}{N_c!(N_m-1)!}$. The number of possible network configurations composed of k branches from these N_b branch configurations is $N_n = \binom{k+N_b-1}{k} = \frac{(k+N_b-1)!}{k!(N_b-1)!}$. This position-agnostic combinatorial expansion leads to a rapidly growing design space, as demonstrated in Figure S11A. For example, for 3 constituent filler concentrations, 220 networks are possible with 3 branches of 3 cells each. This number grows quickly to 53130 networks by increasing the number of branches and cells per branch to just 5 each. Since each candidate network is predicted at negligible computational cost (Figure S11B) and without device-level testing, the model enables systematic exploration of a combinatorial design space containing tens of thousands of architectures (Figure S11A). This allows rapid inverse design towards target behaviors of piezoresistive sensitivity, linearity, and strain range, rather than iterative experimental tuning of individual devices.

2.3. Design of meta strain gauge achieving beyond traditional performance

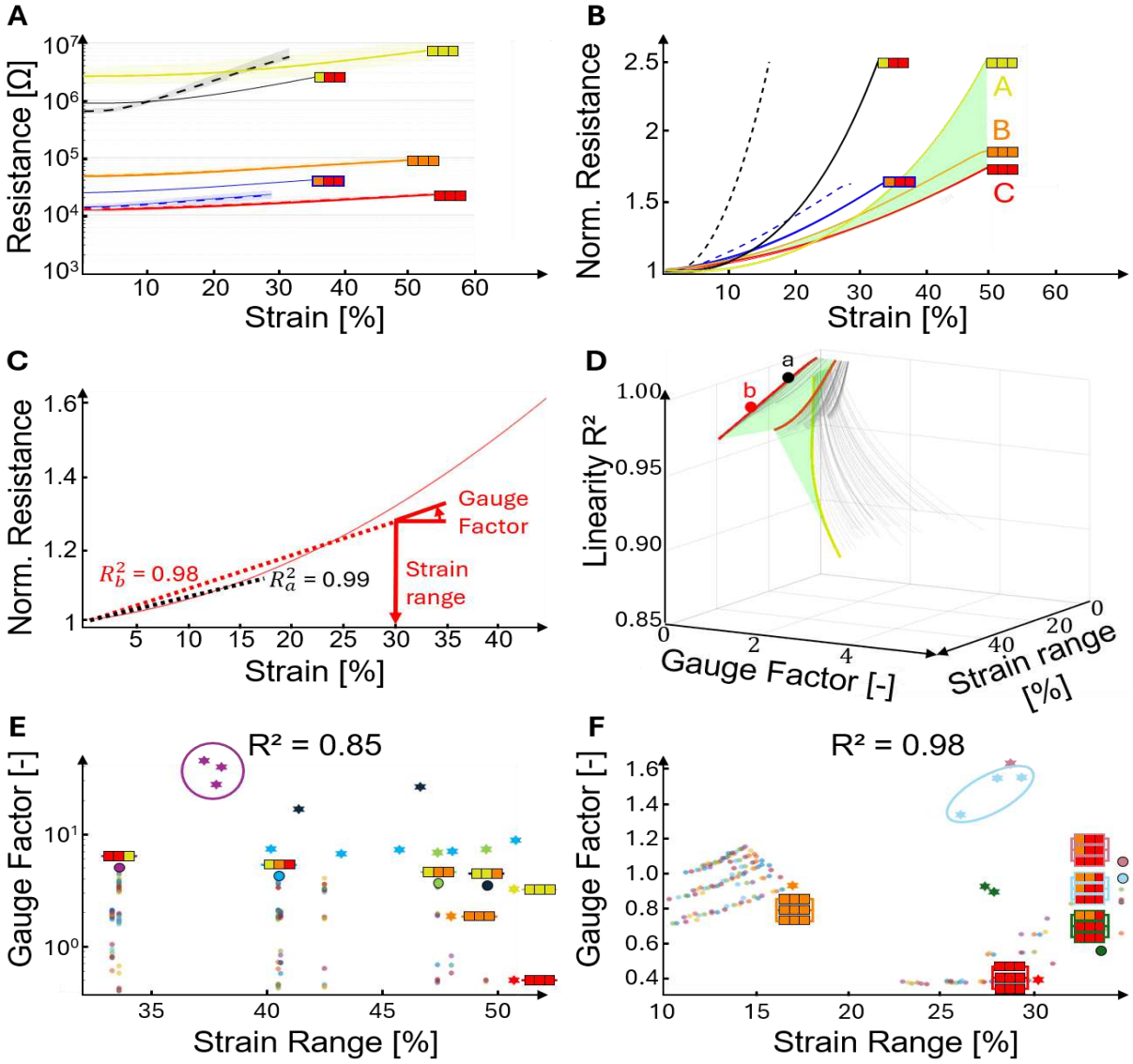

Figure 3. (A,B) Branch electromechanical behavior: The (normalized) resistance $R(\varepsilon)$ of the most sensitive (CAC, black) and most linear (BCC) branch is compared with that of the constituent materials, by experimental measurement (dashed lines with confidence intervals) and model predictions (solid lines). Branch configuration is indicated by the three constituent cells (A: yellow, B: orange, C: red). The shadowed area in panel B defines the performance envelope produced by uniform composites. **(C)** $R/R_0(\varepsilon)$ with linear regressions shown for different linearity (R^2) thresholds, illustrating how gauge factor and strain range are defined and how both increase as the linearity requirement is relaxed. **(D)** Since each regression returns a different *GF* and strain range when the linearity requirement changes, each sensor produces a 3D trajectory in the (ε, *GF*, R^2) space. The regressions of panel C are indicated by the points "a" and "b". The metamaterials unlock performance combinations inaccessible to homogeneous composites (limited to the green space). **(E-F)** The gauge factor and strain range depend on the linearity requirement of the application: High-sensitivity sensing can relax linearity to R^2>0.85 (E), while high linearity requires R^2>0.98 (F). Model predictions (circle markers) were used to select promising sensitive (E) and linear (F) candidates. These candidates (big circle markers, configuration indicated by constituent cells) were experimentally validated (star markers of the same color), and compared to the constituent materials (all cells same color). The most performant metamaterials (encircled) were demonstrated as sensors in the next section.

The central consequence of hierarchical organization is that the metamaterials expand the electromechanical responses beyond the envelope of the homogeneous constituent materials. Figure 3(A,B) and Figure S10 show that both experiment and model capture this behavior, comparing the $R(\varepsilon)$ response by model prediction (solid line) and experiment (dashed line with confidence interval). The $R(\varepsilon)$ curves show an overall agreement between experiment and model, even though conductivity – especially for composites near percolation - varies over orders of magnitude and is more sensitive to structural variations than mechanical response. The normalized $R(\varepsilon)$ curves in Figure 3B are particularly informative, defining response shape and gauge factor. The green envelope indicates the range expected for uniform composites with filler loadings between those of A and C. Both experiment and model show responses outside this envelope, confirming non-averaging behavior beyond simple mixing rules. The network design can tune branch sensitivity outside of this envelope by strain redistribution. Consider the CAC branch (black). Being electrically dominated by material A ($R_{branch} \approx R_A$), the branch sensitivity $\Delta R_{branch}/\varepsilon_{branch}$ is governed by two factors: The sensitivity of material A ($\Delta R_A/\varepsilon_A = GF_A$), and its relative cell strain ($\varepsilon_A/\varepsilon_{branch}$), which is the highest possible when surrounded by stiff C cells. Together, this yields maximum sensitivity that defies conventional mixing rules because the response emerges from cell interactions, rather than from the intrinsic material properties. Unlike homogeneous composites, where blending A with less-sensitive C would reduce sensitivity, the metamaterial achieves a fourfold increase (GF 1.55 vs 0.39) due to strain amplification in A from its interdependence with stiffer C cells.

The model captures the qualitative ranking in sensitivity across branch designs. Quantitatively, however, measured sensitivities are consistently higher than the predicted ones due to strain non-idealities not registered by the model (for example, Figure S9). The model input is taken from experimental measurements of the homogeneous materials (A, B, C) that were printed as single continuous filaments. In contrast, heterogeneous branches (e.g. ABC) are fabricated by sequential deposition of the different cells, with a small partial overlap at their boundaries. These overlapping regions are thicker than the bulk filament, and thus stiffer, provoking extra strain in the bulk regions. Though the model could be improved to account for those thicker overlap regions, the current version provides a proof of concept by reproducing/predicting the qualitative and semi-quantitative (trends) electromechanical behavior across heterogeneous branches. Importantly, the model is universal and physics-based, so it can describe a wide range of systems where functional and mechanical properties interact on the three (cell, branch, and network) levels, where it enables inverse design toward targeted performance.

Sensor performance is evaluated by three key metrics: sensitivity (gauge factor), linearity, and strain range, all derived from linear regression, as shown in Figure 3C (more details in SI6.3). The gauge factor corresponds to the regression slope of the normalized resistance $R/R_0(\varepsilon)$. For a given linearity requirement (e.g., $R^2 = 0.99$), the strain range is defined as the interval over which this criterion is satisfied. Because the $R(\varepsilon)$ response is inherently nonlinear and continuously accelerating, the linearity threshold directly determines the extracted metrics: relaxing the linearity requirement expands the strain range into higher-strain regions where the slope is larger, thereby increasing both strain range and gauge factor. Thus, linearity, sensitivity, and strain range are interdependent, and each sensor presents a limiting trade-off between *GF* and R^2. This trade-off is represented in a continuous trajectory in the $(\varepsilon_{\text{end}}, GF_{\text{fit}}, R^2)$ 3D space, as shown in Figure 3D. Considering the interdependence of the three metrics enables multi-objective optimization to maximize the performance of a given application, according to the specific importance of each metric (Figure S12A)[26]. The analytical model can predict, evaluate, and screen thousands of architectures at negligible computational cost, enabling systematic exploration of huge combinatorial design spaces toward application-specific target responses. This transforms sensor design from costly experimental trial-and-error or data-driven black-box AI optimization into an interpretable inverse design process, in which architecture-performance relationships are directly linked to underlying physical mechanisms. The metamaterial architectures describe trajectories in the $(\varepsilon_{\text{end}}, GF_{\text{fit}}, R^2)$ 3D space, which appear clustered into three distinct groups around each constituent material trajectory. Interestingly, Figure 3D and Figure S12 show that the metamaterials access performance combinations beyond the envelope of the homogeneous constituent materials (the green envelope), breaking the traditional trade-off between linearity and sensitivity. Importantly, the significance of this expanded space lies in enabling application-specific electromechanical functionality rather than identifying a single optimal architecture.

While demonstrated for in-plane PDMS/CNT piezoresistive sensing, the metamaterial design framework is material- and functionality-agnostic, enabling applications beyond strain sensing such as stretchable transistors and other architected electromechanical devices. Alternate sensing modes are supported by changing mechanical loading (in-plane strain or through-plane compression) and electrical output (in-plane resistance R_{ip}, through-plane resistance R_{tp} or through-plane capacitance C_{tp}). The model extends naturally by: (i) extracting the appropriate constitutive curves (e.g. $R_{tp}(\varepsilon)$ or $C_{tp}(\varepsilon)$) of the constituent materials; and (ii) adapting the physical laws for mechanical loading and electrical output as summarized in Table S2.

Metamaterials in through-plane piezoresistive (R_{tp}, Figure S13) and piezocapacitive (C_{tp}, Figure S14) modes reveal unconventional behavior, with designs operating outside the envelope of the constituent materials. Through-plane sensing escapes the envelope by trading enhanced linearity (R^2>0.98) for reduced sensitivity, with a maximum GF of 1.2 (C_{tp}) and -0.5 (R_{tp}) at the maximum strain range ε_{end}. This behavior arises from the physical laws: Through-plane sensing is dominated by the cell with the lowest resistance ($R_{branch}^{-1} = \sum R_{cell}^{-1}$) and highest capacitance ($C_{branch} = \sum C_{cell}$), which corresponds to the C material. Thus, the electrically dominant C material (the stiffest) undergoes strain reduction, reducing sensitivity but increasing linearity. Those features are desirable for ultra-linear sensors, or strain-insensitive materials for stretchable electronics (interconnects, amplifiers,…).

The situation of through-plane modes contrasts with in-plane sensing, where the electrically dominant A cell (the softest) undergoes strain amplification, enhancing sensitivity. Importantly, in-plane resistance sensing also escapes the linearity envelope, being able to combine enhanced linearity with enhanced sensitivity. Thus, the in-plane resistance mode proves most suitable for sensing applications, offering a wider range of behaviors and superior sensitivity beyond the envelope. Model predictions of the meta gauges (circle markers in Figure 3E, F) showed performance gains over the constituent material (star markers for A-yellow, B-orange, C-red). Figure 3E presents the performance for high-sensitivity operation where linearity is of lower importance (R^2>0.85). The best predicted meta gauges (large circle markers, with their configuration indicated by their constituent cells) are single branches because – unlike the interdependent cells in a branch that produce strain amplification – branches behave independently, so combining them in parallel has an averaging effect that dilutes the sensitivity of the most sensitive branch. These meta gauges were experimentally tested (star marker of the same color) and consistently demonstrated higher sensitivity than the most sensitive constituent material (A, the yellow star with a *GF* of 3.59). For instance, the ABB branch (green circles) predicted a higher *GF* than A, and it demonstrated experimentally double the sensitivity (*GF* 7.11) for a similar strain range of 50%. The CAC branch (purple) offered a tenfold increase in sensitivity (reaching a *GF* of 37.5) for a modest reduction in strain range (38%). Figure 3F presents the performance for high linearity sensing (R^2>0.98). The meta gauges generally achieved higher sensitivity for a similar strain range, e.g., the CCC//BCC//BBC sensor (called ‘S’, light blue) achieved a four-fold sensitivity increase (*GF* 1.55 vs 0.39) over the most linear constituent material (C, red star).

2.4. Real-time on-body testing of metamaterial sensors and constituent materials

As a proof of concept, the real-world sensing performance of the most sensitive (CAC branch, purple in Figure 3E) and most linear (S sensor, blue in Figure 3F) meta-gauges was compared to their counterpart composites (A and C), by monitoring respiratory strain in real time. The sensors were mounted in a clamping fixture around the thorax to monitor chest expansion during breathing (Figure 4A). Figure 4B shows their synchronized resistance and strain signals (more info on this method in SI8, video SI2). Non-linearity manifests as a systematic deviation, where resistance falls below the strain signal at low strains but rises above it at higher strains. The $R(\varepsilon)$ curves in Figure 4C highlight each sensor's sensitivity (slope), linearity (curvature), and variability (shaded 95% prediction intervals).

The CAC metamaterial had the highest sensitivity, increasing resistance by 20% at 10% strain (compared to 11% for the most sensitive homogeneous material A). The S metamaterial shows the greatest linearity, maintaining the closest one-to-one correspondence between strain and R/R_0. It also has 50% higher sensitivity than the most linear homogeneous material C, increasing R/R_0 by 3.6% versus 2.4% at 10% strain. This comparison reflects each material's intrinsic sensitivity and linearity, revealing that their trade-off relaxed for the metamaterials and demonstrating how architectural design, not only material properties, dictates performance.

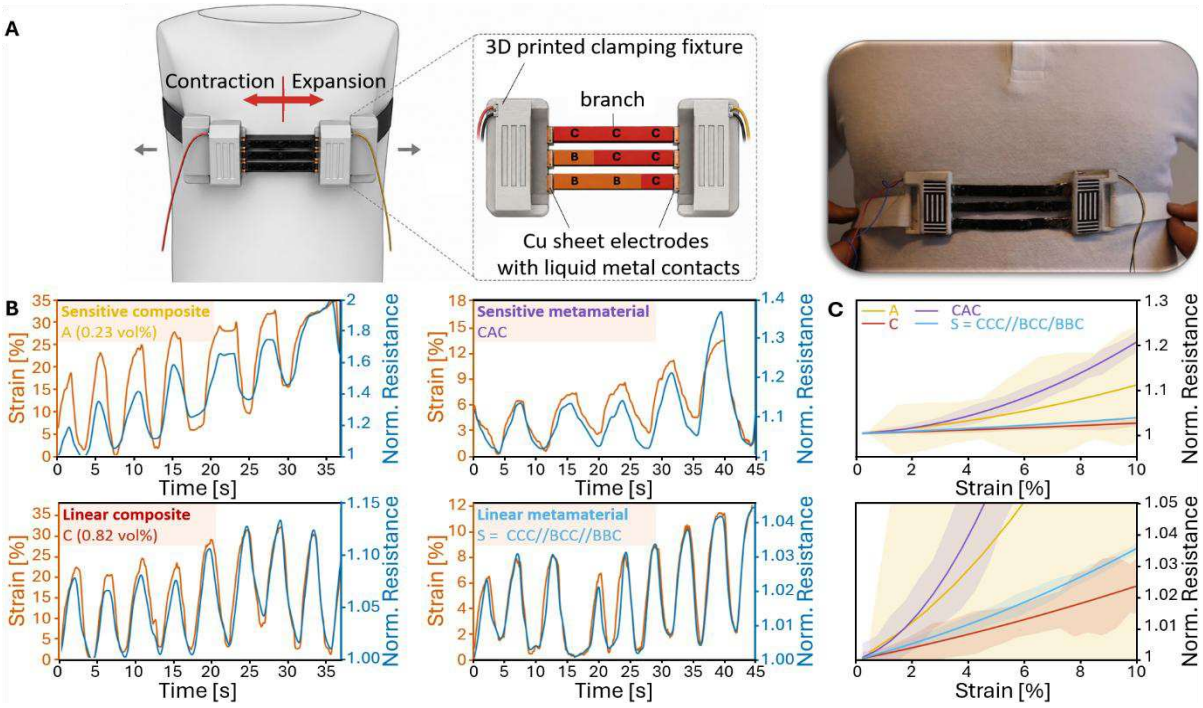

Figure 4. Real-world validation of model-predicted metamaterials for on-body respiratory monitoring, comparing metamaterials (CAC, S) and their counterpart composites (A, C). **(A)** Wearable sensor mounted in the fixture on a strap around the thorax. **(B)** Real-time strain and resistance signals, showing higher sensitivity for the metamaterials and higher linearity for the linear-optimized S sensor. **(C)** Representative $R(\varepsilon)$ regression curve of each sensor at 2 scales. The raw data and regression fit are provided in Figure S15.

3. Materials and Methods

Ink formulation. Inks were prepared by dispersing CNTs (NC7000, Nanocyl S.A., Belgium) into a PDMS matrix (Sylgard 184, Dow Corning, USA) using THF (>99.9%, Sigma-Aldrich, USA) solvent. PDMS component A was dissolved in THF, after which CNTs were dispersed using an ultrasonic probe (UP 400S, Hielscher Ultrasonics GmbH, Germany) in three intervals: 30 m, 85% power, 0.8 cycle; 30 m, 80% power, 0.9 cycle; 10 m, 85% power, continuous. THF was removed with a rotary evaporator (Büchi R215, 15 rpm, 300 mbar, 50 °C), and then the PDMS curing agent was mixed (10:1 base:crosslinker). Three CNT loadings —0.23, 0.55, and 0.82 vol%—were formulated as the constituent materials A, B, and C for printing.

Rheology. Rheology of the CNT/PDMS inks was measured on a rotational rheometer (MCR501, Anton Paar, Austria) using a 25 mm plate–plate geometry and a gap of 1 mm. Shear-rate sweeps measured viscosity and shear stress as a function of shear rate over the printing-relevant range, and oscillatory strain sweeps were conducted to determine storage (G′) and loss (G″) moduli. More detailed analysis of rheology data and DIW applicability in SI4.

Direct ink writing of graded architectures. Branches and networks were fabricated using a modified Ender 3 V3 system (Creality, China) equipped with 14-gauge nozzles (Ø 1.63 mm) and a 60 °C heated glass substrate. Homogeneous branches (AAA, BBB, CCC) were printed in a single continuous pass, while heterogeneous branches (e.g., ABC) were printed cell-by-cell by switching between inks, using a 0.5 mm overlap to ensure filament continuity. Each branch consisted of three cells of equal length (30 mm), with an additional 15 mm on the outer cells to allow mechanical clamping during testing. After thermal curing, printed branches were cut into 10 mm-wide strips for mechanical, electrical, and electromechanical characterization.

Electromechanical characterization. Mechanical Uniaxial tensile testing was performed according to ASTM D638 (Instron 5943, strain rate 0.5 % s^{-1}, air-pressure grips at 2 atm).
Electrical resistance was recorded during mechanical loading using a four-wire configuration (Keysight B2961B source meter, 10 µA). Gold-sputtered end contacts covered with liquid metal (Galinstan) ensured low-impedance electrical connection to the copper sheets that were embedded in the clamps, as shown in Figure S5. Mechanical and electrical systems were triggered simultaneously for a common time reference, enabling acquisition of synchronized $\sigma(\varepsilon)$ and $R(\varepsilon)$ curves for each sample (Figure S6). The procedures to convert this experimental data into analytical constitutive inputs for the hierarchical model are provided in SI6.1.

Model. The analytical, physics-based model was developed to propagate cell behavior through hierarchical networks; more details on the model development, validation, and performance screening for in-plane piezoresistive sensing are provided in SI6.2-SI6.3. The analytical model is not limited to piezoresistive sensing but is a universal framework for hierarchical systems, and was extended to alternate sensing modes in SI7.

4. Conclusion

This work introduced architected aperiodic metamaterials - a new class of hierarchical composites with tailored responses that arise from structural organization, rather than intrinsic material properties. By discretizing nanocomposites into cells with distinct filler concentrations and electromechanical behaviors, a network of interdependent cells was designed that unlocked combinations of sensitivity, linearity, and strain range inaccessible to uniform composites, expanding the performance space. This demonstrated global strain sensing as an emergent, network-level property arising from interactions between interdependent constituents, that can be engineered through architecture rather than intrinsic material properties, representing a paradigm shift: from material composition optimization to network design.

The physics-based hierarchical framework provides a universal tool for rational inverse design of architected metamaterials with tailored responses. It maps how cell behavior propagates through the hierarchy, grounded in well-established physical laws to enable accurate prediction and a mechanistic insight. It enables efficient exploration of large architectural design spaces through prediction rather than costly trial-and-error experimentation, systematically mapping and navigating the expanded performance space of the metamaterials to identify architectures with targeted electromechanical responses. Experimental validation confirmed that metamaterials expand the performance space (enhancing sensitivity while preserving extreme linearity over a large strain range) and improved proof-of-concept respiratory monitoring. Crucially, the value of the framework does not lie in maximizing a single metric such as gauge factor, but in navigating regions of performance space that became accessible through hierarchical organization. Different applications require different electromechanical responses, ranging from highly sensitive strain sensing to strain-invariant electrical functionality, and may even rely on different electromechanical transduction mechanisms. The framework enables systematic exploration of a multidimensional performance space, identifying architectures with tailored, application-specific electromechanical responses. Furthermore, it is not limited to CNT/PDMS materials or piezoresistive sensing, and can be applied to any hierarchical system where mechanical and functional properties interact through known physical laws.

Together, these advances establish hierarchical composites as a powerful platform for inverse design of electromechanical functionality, encoded through architecture. This paradigm shift – from material composition optimization to network design – opens opportunities for rationally engineered soft electronic systems beyond piezoresistive strain sensing, where targeted performance is dictated by structural organization.

References

1. Kaidarova, A. *et al.* Hybrid organic-inorganic functional nanocomposites: From basis to applications in stretchable sensing and energy devices. *Materials Science and Engineering: R: Reports* **163**, 100933 (2025).
2. Souri, H. *et al.* Wearable and Stretchable Strain Sensors: Materials, Sensing Mechanisms, and Applications. *Advanced Intelligent Systems* **2**, (2020).
3. Amjadi, M., Kyung, K., Park, I. & Sitti, M. Stretchable, Skin-Mountable, and Wearable Strain Sensors and Their Potential Applications: A Review. *Adv. Funct. Mater.* **26**, 1678–1698 (2016).
4. Du, J. *et al.* Optimized CNT-PDMS Flexible Composite for Attachable Health-Care Device. *Sensors* **20**, 4523 (2020).
5. Duan, L., D'hooge, D. R. & Cardon, L. Recent progress on flexible and stretchable piezoresistive strain sensors: From design to application. *Prog. Mater. Sci.* **114**, 100617 (2020).
6. Morgan, L. E., Nelson, B. L., Titman, A. C. & Worthington, D. J. Detecting bias due to input modelling in computer simulation. *Eur. J. Oper. Res.* **279**, 869–881 (2019).
7. Monnens, W. *et al.* Scalable Electrodeposition of Liquid Metal from an Acetonitrile-Based Electrolyte for Highly Integrated Stretchable Electronics. *Advanced Materials* **35**, (2023).
8. Du, J. *et al.* Optimized CNT-PDMS Flexible Composite for Attachable Health-Care Device. *Sensors* **20**, 4523 (2020).
9. Garcia, J. R., O'Suilleabhain, D., Kaur, H. & Coleman, J. N. A Simple Model Relating Gauge Factor to Filler Loading in Nanocomposite Strain Sensors. *ACS Appl. Nano Mater.* **4**, 2876–2886 (2021).
10. Wang, R. *et al.* Carbon Nanotube-Based Strain Sensors: Structures, Fabrication, and Applications. *Adv. Mater. Technol.* **8**, (2023).
11. Huang, X., Yin, Z. & Wu, H. Structural Engineering for High-Performance Flexible and Stretchable Strain Sensors. *Advanced Intelligent Systems* **3**, (2021).
12. Wang, X., Li, J., Song, H., Huang, H. & Gou, J. Highly Stretchable and Wearable Strain Sensor Based on Printable Carbon Nanotube Layers/Polydimethylsiloxane Composites with Adjustable Sensitivity. *ACS Appl. Mater. Interfaces* **10**, 7371–7380 (2018).
13. Wang, Y. *et al.* Super-Elastic Graphene Ripples for Flexible Strain Sensors. *ACS Nano* **5**, 3645–3650 (2011).

14. Chen, J., Zhu, Y. & Jiang, W. A stretchable and transparent strain sensor based on sandwich-like PDMS/CNTs/PDMS composite containing an ultrathin conductive CNT layer. *Compos. Sci. Technol.* **186**, 107938 (2020).

15. Lu, N., Lu, C., Yang, S. & Rogers, J. Highly Sensitive Skin-Mountable Strain Gauges Based Entirely on Elastomers. *Adv. Funct. Mater.* **22**, 4044–4050 (2012).

16. Luo, Y. *et al.* Technology Roadmap for Flexible Sensors. *ACS Nano* **17**, 5211–5295 (2023).

17. de Souza Oliveira, H. *et al.* Mechanical metamaterial sensors: from design to applications. *J. Phys. D Appl. Phys.* **58**, 133002 (2025).

18. Dong, S. & Hu, H. Sensors Based on Auxetic Materials and Structures: A Review. *Materials* **16**, 3603 (2023).

19. Hu, T. *et al.* Omnidirectional Configuration of Stretchable Strain Sensor Enabled by the Strain Engineering with Chiral Auxetic Metamaterial. *ACS Nano* **17**, 22035–22045 (2023).

20. Jiang, Y. *et al.* Auxetic Mechanical Metamaterials to Enhance Sensitivity of Stretchable Strain Sensors. *Advanced Materials* **30**, (2018).

21. Wang, J. *et al.* Strain-invariant conductance in an elastomeric nanocomposite mesh conductor for stretchable electronics. *J. Mater. Chem. C Mater.* **8**, 9440–9448 (2020).

22. Hong, L., Zhang, H., Kraus, T. & Jiao, P. Ultra-Stretchable Kirigami Piezo-Metamaterials for Sensing Coupled Large Deformations. *Advanced Science* **11**, (2024).

23. De Smedt, S., Dong, Q., Molina-Lopez, F. & Cardinaels, R. A high-throughput method to determine the electrical percolation threshold of conductive polymer nanocomposite inks via gradient direct ink writing. *Composites Communications* **65**, 102850 (2026).

24. De Smedt, S., Attaianese, B. & Cardinaels, R. Direct ink writing of particle-based multiphase materials: From rheology to functionality. *Curr. Opin. Colloid Interface Sci.* **75**, 101889 (2025).

25. Wang, Z. *et al.* Electromechanics of stretchable hybrid response pressure sensors based on porous nanocomposites. *J. Mech. Phys. Solids* **193**, 105872 (2024).

26. Nittala, A. S., Karrenbauer, A., Khan, A., Kraus, T. & Steimle, J. Computational design and optimization of electro-physiological sensors. *Nat. Commun.* **12**, 6351 (2021).

27. Wang, Y. *et al.* Fabrication of ultra-high working range strain sensor using carboxyl CNTs coated electrospun TPU assisted with dopamine. *Appl. Surf. Sci.* **566**, 150705 (2021).

28. Srivastava, A. & Klassen, E. P. *Functional and Shape Data Analysis*. (Springer New York, New York, NY, 2016). doi:10.1007/978-1-4939-4020-2.

Supporting Information

Overcoming conventional trade-offs in strain sensing with physics-guided inverse design of aperiodic architected nanocomposites

V. Naenen, S. De Smedt, A. Kaidarova, R. Cardinaels, F. Molina-Lopez
Department of Materials Engineering, KU Leuven, Kasteelpark Arenberg 44, 3001, Leuven, Belgium.
E-mail: francisco.molinalopez@kuleuven.be

SI1.Strain sensing performance

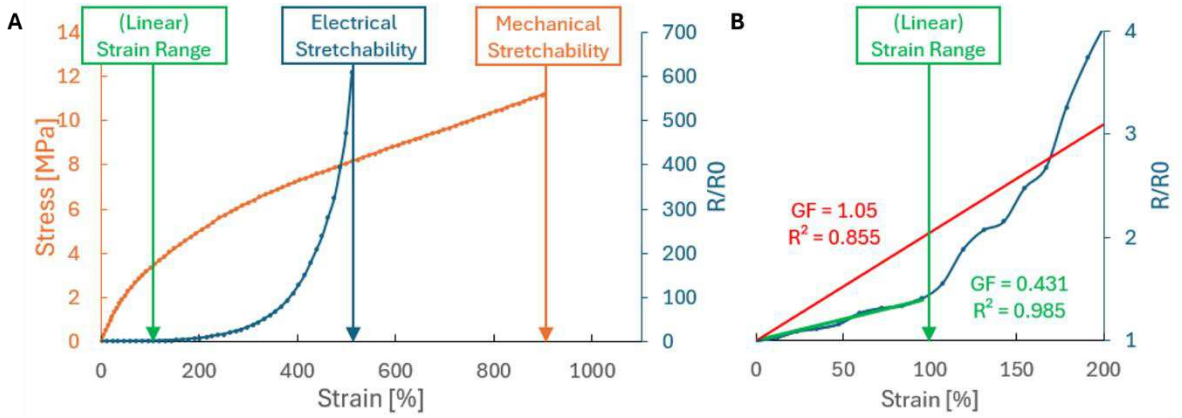

Figure S1. (A) Sensing behavior comprises the mechanical (stress, orange) and electrical (normalized resistance, blue) behavior[27]. When stretchability is reported, it might refer to mechanical stretchability (maximum observable strain before mechanical fracture) or electrical stretchability (maximum observable strain before an electrical open circuit, e. g. due to fracture of the percolation network). **(B)** When considering the inherently non-linear electrical behavior, a smaller strain range can be defined where the electrical behavior is sufficiently linear (e.g. R^2 above 0.98), giving the linear strain range. For comparison, the linear fitting of the same curve for less stringent linearity (R^2 above 0.85) is represented in red, demonstrating larger strain range and sensitivity.

SI2.Theory on Linearity of Percolated Nanocomposites

The $R(\varepsilon)$ response of percolated composites has unavoidable nonlinearity, arising from:
(1) **geometric changes** in sample dimensions (Pouillet's effect)
(2) **changes in intrinsic resistivity** due to strain-induced modification of tunneling distances within the conductive network.

SI2.1.Geometric contribution (Pouillet effect)

For an unstrained sample, the electrical resistance is

$$R_0 = \frac{\rho_0 L_0}{T_0 W_0}. \quad \text{(Eq. S1)}$$

Here, ρ_0, L_0, T_0, W_0 are the unstrained resistivity, length, thickness and width.

When uniaxial strain ε is applied along the length, the strained dimensions (denoted by ') are

$$L' = L_0(1+\varepsilon), T' = T_0(1+\varepsilon)^{-\nu}, W' = W_0(1+\varepsilon)^{-\nu}, \quad \text{(Eq. S2)}$$

where ν is the Poisson ratio.

The strained resistance is

$$R' = \frac{\rho' L'}{T' W'}, \text{ with } \rho' \text{ the resistivity.} \quad \text{(Eq. S3)}$$

Normalizing by the unstrained resistance gives

$$\frac{R'}{R_0} = \frac{\rho'}{\rho_0}(1+\varepsilon)^{1+2\nu}. \quad \text{(Eq. S4)}$$

For incompressible materials, such as elastomeric matrices ($\nu \approx 0.5$):

$$\frac{R'}{R_0} = \frac{\rho'}{\rho_0}(1+\varepsilon)^2. \quad \text{(Eq. S5)}$$

As a consequence, even if resistivity were constant, the geometric term $(1+\varepsilon)^2$ already produces a nonlinear resistance–strain response.

SI2.2.Tunneling contribution

In percolated nanocomposites, resistivity also changes with strain due to changes to the tunneling between adjacent conductive fillers. The tunneling-dependent resistivity is

$$\rho'(d) = Ae^{\beta d}, \quad \text{(Eq. S6)}$$

where d is the interparticle separation, A a pre-factor, and $\beta = \frac{2}{\hbar}\sqrt{2m\phi}$ is a tunneling decay constant that depends on electron mass m and barrier height ϕ.

The normalized resistivity scales as

$$\frac{\rho'}{\rho_0} \sim e^{\beta(d-d_0)}. \quad \text{(Eq. S7)}$$

Thus, both ρ'/ρ_0 and its derivative are exponential in nature, adding a second, strongly nonlinear contribution to resistance under strain.

Conclusion. Both the geometric term $(1+\varepsilon)^{1+2\nu}$and tunneling-controlled resistivity term $e^{\beta(d-d_0)}$ introduce inherent nonlinearity. In real percolated nanocomposites, the exponential tunneling contribution amplifies the geometrical quadratic behavior, making nonlinear resistance–strain $R(\varepsilon)$ curves an intrinsic feature of the material system.

SI3.Benchmarking

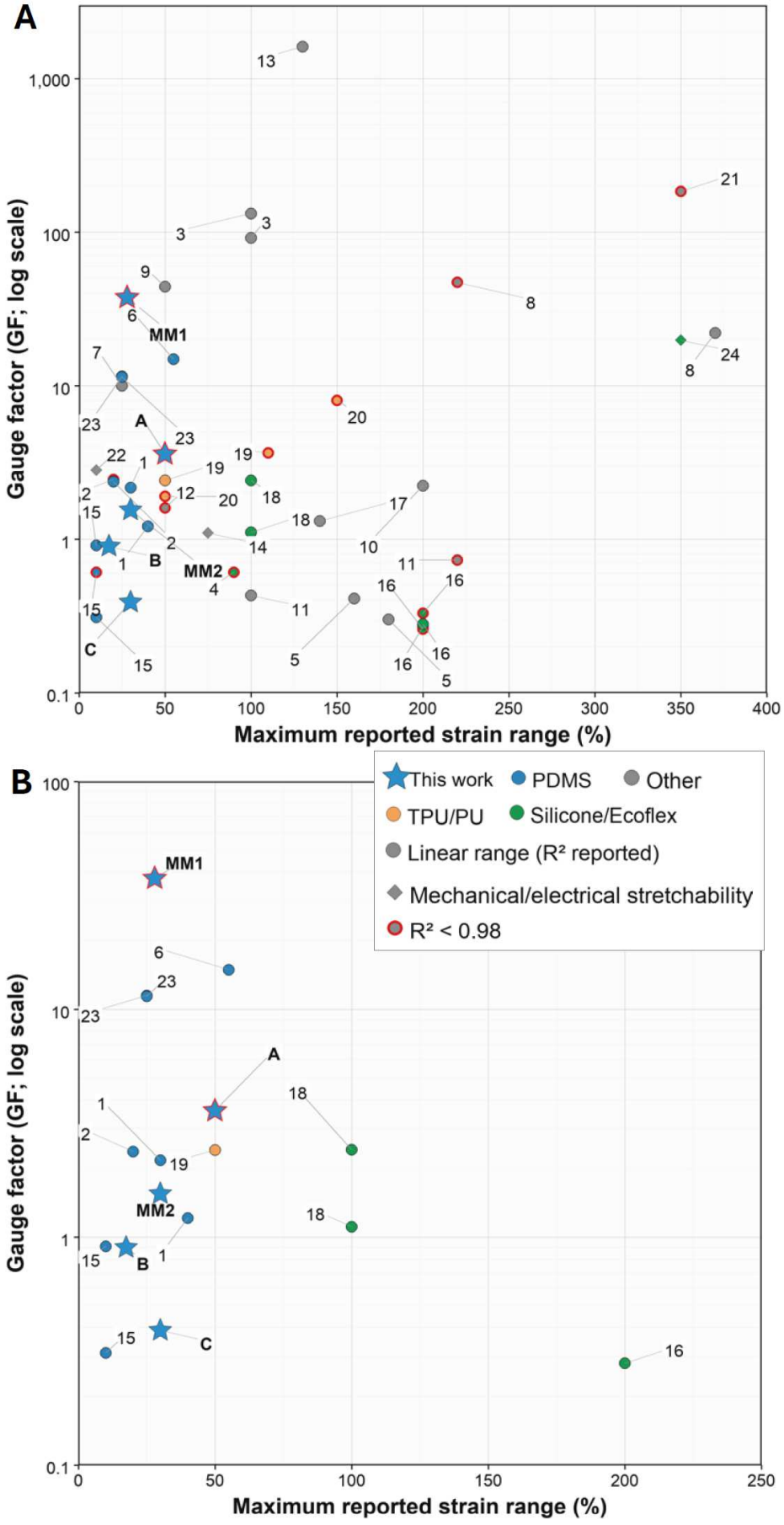

Figure S2. Literature comparison of *GF*, strain range and linearity. (**A)** All reported sensors. Circles denote linear strain ranges evaluated using the definition adopted in this manuscript (the strain interval starting at 0%, where linear regression has a sufficiently large R^2 value), whereas diamonds denote the maximum mechanical or electrical stretchability reported (see Fig. S1). Colors indicate sensor class. "Other" comprises non-bulk sensor architectures, including CNT coatings deposited on substrates and electrospun fibrous mats containing ultrasonically embedded CNTs. These exotic sensor architectures can demonstrate superior sensitivity but often struggle with difficult processability, scalability or environmental stability. Moreover, their behavior is highly material- and architecture-specific, not allowing for versatility in tailoring the performance towards other applications, nor the accurate prediction of their behavior for modified architectures or for alternate sensing modes. Red outlines identify values with poor linearity ($R^2 < 0.98$). Numbers correspond to the references in Table S1. This work (blue star markers) consists of 2 classes of PDMS-based nanocomposites: the representative metamaterials (MM1 and MM2) generally show enhanced sensitivity for a similar strain range and linearity compared to the homogeneous composites (A,B,C) that they are made of. (**B)** Only nanocomposite sensors (no 'other' architectures).

Table S1. Benchmarking of CNT-based longitudinal piezoresistive strain sensors.

Material system / composition	Strain range	GF	R^2	Fabrication method	Ref.
MetaMaterial (MM) MM1 = CAC MM2 = CCC//CCB//CBB	 28% 30%	 37.5 1.55	 >0.85 >0.98	Direct Ink Writing (DIW) of concentration-graded CNT/PDMS inks	This work
Starting material (CNT/PDMS) A = 0.23vol% B = 0.52 vol% C = 0.82 vol%	 50% 17% 30%	 3.59 0.9 0.39	 0.85 0.98 0.98		
CNT/PDMS	30% 40%	2.17 1.21	0.987 0.992	Solution blending + mold casting/curing	1
CB–CNT/PDMS	20% 20%	2.45 2.37	0.972 0.988	Hybrid filler dispersion (n-hexane) + casting on geotextile fabric	2
CNT/PDMS	100% 100%	132 91.8	0.993 0.991	Self-segregated CNT/PDMS dip-coat onto elastic medical bandage	3
CNT/Ecoflex	90%*	0.61*	>0.97*	Solution mixing + printing into silicone substrate	4
CNT fiber /Ecoflex	160% 180%	0.41 0.3	>0.99 >0.99	Dry-spinning of CNT fiber from CNT forest, transferred to Ecoflex	5
Ag@CNT/PDMS	55%*	14.9*	>0.98*	Template method (dip-coating CNT/Ag network into PDMS mold)	6
CNT/TPU	25%	≈ 10	>0.98	Electrospun wavy TPU fiber + CNT deposition	7
CNTs (P-DATPU/CNTs) /Dopamine-mod. TPU	370% 220%	22.0 47.1	0.997 >0.9	Electrospinning + dopamine functionalization + suction filtration of CNTs	8
CNT@AgNPs/ TPU	50%*	44.1*	>0.98*	Electrospinning + dip-coat CNT + in-situ AgNO3	9
CNT-Ppy/ WSP	200%*	2.23*	>0.98*	CNT dip-coat + in-situ PPy polymization on fabric	10
CNT/ Dopamine-mod. TPU(DATPU/CNTs)	100%* 220%*	0.43* 0.73*	>0.98* >0.97*	Electrospinning + dopamine modification + ultrasonication-assisted CNT deposition	11
CNT/TPU	50%*	1.6*	0.97*	Electrospun TPU film + dip-coat ultrasound CNT	12
MWCNTs yarn/ Dopamine-mod. SEBS/	130%*	1612*	0.99*	Electrospun SEBS yarn + dopamine modification + CNT coating, twisted into yarn	13
Carbon nano-onion + CNT / SEBS	75%	~1.1	-	Solution-processed all-carbon ink, dip/blade-coated	14
CNT@CNC/PDMS	10% 10%	0.91 0.31	0.99 0.99	Sustainable emulsion method; segregated structure around PDMS microspheres	15
MWCNT/Ecoflex	~200%* ~200%*	0.33* 0.28*	0.916* 0.985*	Solution mixing/casting of MWCNT/Ecoflex composite	16
MWNT/SWNT/ TPU yarn	140%*	1.31*	0.994*	Electrospun TPU fiber yarn decorated with CNTs	17
CNT / silicone rubber	100% 100%	2.42 1.11	0.990 0.984	CNT network embedded in silicone rubber thin film	18
CNT/TPU	110%* 50%*	3.65* 2.41*	0.97* 0.99*	Templated porous CPC with microdome surface (TPU + CNT)	19
CNT/rGO core-sheath fiber /PU	50%* 150%*	1.90* 6.18*	0.93* 0.9*	Coaxial wet-spinning, encapsulated core-sheath fiber	20
CNT/MXene/TPU	350%	184	<0.9	Multilayer electrospin + spray (brick-and-mortar)	21
CNT/ Waterborne-PU (WPU-BP)	10%	2.82	-	Vacuum filtration of WPU- CNT buckypaper	22
MWCNT/CB/PDMS	25%*	11.41*	0.999*	Solution blend and molding of ternary composite	23
CNT/liquid-metal/Fe-powder/Ecoflex	40%	4	0.989	Direct Ink Writing (DIW) / 4D printing	24
Aligned CNT film	280% (fracture)	0.04	-	Aligned CVD- CNT film, fractured under stretch	25

*Self-calculated values. Linear regression was performed over progressively increasing strain ranges until $R^2 < 0.98$. The GF and the corresponding strain range satisfying $R^2 < 0.98$ are reported. Grey shading denotes textile-/bandage-architectured sensors.

SI4.Rheological properties relevant for DIW printing

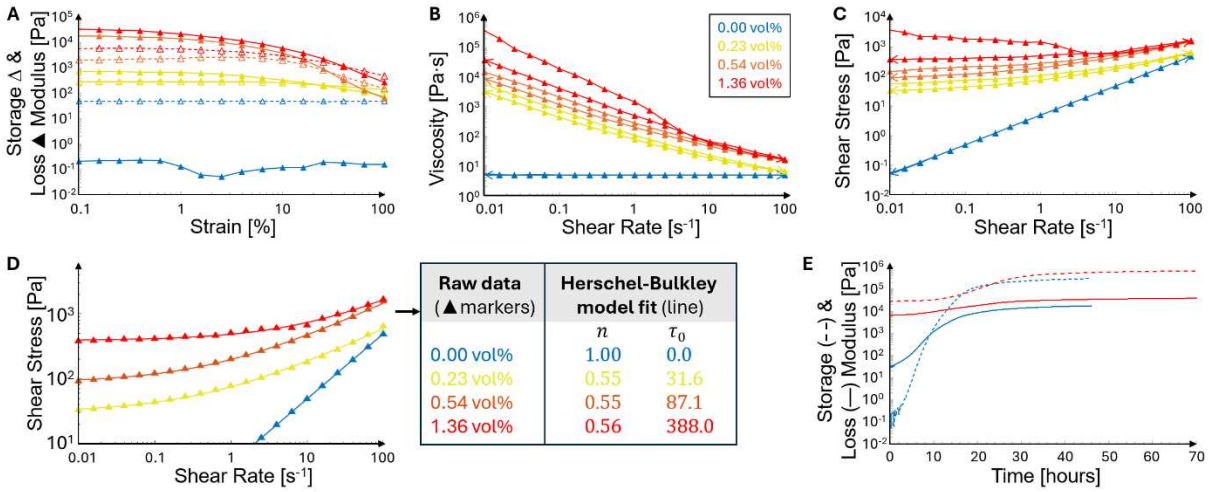

Figure S3. Rheology study of CNT-PDMS inks. **(A)** Strain amplitude sweeps to determine the LVR; **(B)** Flow curve of viscosity vs. shear rate, showing both up- and downwards ramps; **(C,D)** Flow curve of shear stress vs. shear rate (up- and downwards ramps), and the Herschel-Bulkley model fits; **(E)** Time sweep to characterize curing kinetics.

Rheological measurements (Figure S3) were used to evaluate whether the inks satisfy the key requirements for DIW printing: (i) a measurable linear viscoelastic region (LVR) for predictable ink behavior under printing-relevant deformation, (ii) shear-thinning for easy extrusion, (iii) a finite yield stress for shape retention, and (iv) curing kinetics compatible with layer-by-layer deposition[24].

(i) Linear viscoelastic region (LVR). The strain-amplitude sweeps in Figure S3A provide insight into the LVR at small strains, where storage and loss moduli (*G'* and *G"*) are constant. Pure PDMS exhibits liquid-like behavior across the entire strain range, with $G' < G''$ and both moduli remaining nearly constant up to 100 % strain. In contrast, the composite inks display a reduced LVR in which G' remains constant and exceeds G'', followed by a sharp decrease in G' as the applied strain disrupts the percolated CNT network. The extent of the LVR further decreases with CNT loading: the 0.23 vol% ink maintains linear behavior up to several percent strain, whereas the 0.55 vol% and 0.82 vol% inks show LVR limits near ~1 % strain. This trend is characteristic of nanocomposite systems, in which stronger filler networks undergo earlier structural breakdown with increasing deformation. A strain amplitude of 0.5 % was thus selected for all frequency sweeps to ensure measurements were performed well within the LVR.

(ii) Shear-thinning behavior for extrusion. The shear-rate sweeps in Figure S3B showed that whereas PDMS ink viscosity was constant, as expected for a Newtonian fluid, all the composite inks exhibited pronounced shear-thinning, with viscosity decreasing by one to two orders of magnitude across the printing-relevant shear-rate range (10-100 s^{-1}). This behavior is essential

for DIW: the ink must flow easily through the nozzle under high shear, yet recover to a high viscosity that hinders flow immediately after deposition.

At low shear rates (< 0.1 s^{-1}), viscosity increases strongly with CNT loading, reflecting the formation of a progressively stronger filler network. The 0.23 vol% ink shows the onset of network formation, whereas the 0.55 vol% and 0.82 vol% inks exhibit much higher zero-shear viscosities, consistent with a percolated microstructure. As shear rate increases, inks thin rapidly to viscosities suitable for extrusion through a 1.63 mm nozzle (10-200 Pa·s).

The shear-stress curves in Figure S3B show smooth, monotonic behavior with minimal hysteresis between upward and downward sweeps (especially below filler concentration of 1.36 vol%), indicating limited thixotropy – the CNT network rebuilds rapidly after shear cessation, which is critical for maintaining filament shape during DIW.

(iii) Yield stress for shape retention. The shear-stress curves of the inks (Figure S3C) exhibit two characteristic regions: a low-shear plateau, where stress remains nearly constant, and a flow regime, where stress increases consistently with shear rate. These regions are described by the Herschel–Bulkley model (Figure S3D)

$$\tau = \tau_0 + k\dot{\gamma}^{\,n}, \qquad \text{(Eq. S8)}$$

where τ is the shear stress, τ_0 the yield stress, $\dot{\gamma}$ the shear rate, k is the consistency index, and n is the flow index. Taking the decimal logarithm and distinguishing between low and high shear rate regimes, we have:

$$log_{10}\,\tau \sim log_{10}\,\tau_0 = constant \qquad \textit{(for small } \dot{\gamma}\textit{)} \qquad \text{(Eq. S9)}$$

$$log_{10}\,\tau \sim n\,log_{10}\,\dot{\gamma} + constant' \qquad \textit{(for large } \dot{\gamma}\textit{)} \qquad \text{(Eq. S10)}$$

From there, it can be seen that the plateau height corresponds to the yield stress τ_0 and the slope of the flow regime corresponds to the flow index n. τ_0 increases sharply with CNT loading, from 0 Pa for pure PDMS to 30 Pa (0.23 vol%), 87 Pa (0.54 vol%), and 338 Pa (1.36 vol%, downward sweep curve). These values demonstrate the formation and progressive strengthening of a percolated CNT network. The yield stress falls within the range required for DIW (10^2–10^3 Pa) to ensure filament stability, shape retention, and resistance to gravitational collapse.

The flow regime reveals the material's behavior once yielding has occurred. Pure PDMS shows $n \approx 1$, confirming Newtonian liquid behavior and explaining its inability to retain shape after DIW. In contrast, all composite inks exhibits $n \approx 0.55$, indicating pronounced shear-thinning

(n < 1): the inks thin rapidly under extrusion-level shear rates (10-100 s^{-1}), enabling smooth flow through the nozzle while maintaining solid-like behavior at rest. This combination of finite yield stress and low flow index is ideal for DIW printing.

Oscillatory frequency sweeps (Figure 1F) corroborate this interpretation: composite inks show a frequency-independent G'plateau with $G' > G''$, consistent with a percolated elastic network capable of sustaining a finite yield stress, whereas pure PDMS remains liquid-like with $G' < G''$. The flow point corresponds to the strain amplitude at which $G' = G''$.

(iv) Curing kinetics compatible with layer-by-layer deposition. Curing behavior was evaluated through time sweeps at 10 rad s^{-1} and 0.5 % strain (Figure S3E). Pure PDMS shows a G'–G''crossover at ~9 h and reaches a plateau after ~30 h. In contrast, the composite inks are solid-like from the start (no crossover), reflecting the reinforcing effect of the MWCNT network, and reach their plateau after ~40 h, indicating a cross-linking delay induced by the presence of the fillers. At elevated temperatures (50–80 °C), curing accelerates to timescales of minutes. This motivated the use of a 60 °C heated print bed, which ensures rapid interlayer bonding and structural stabilization without premature curing inside the nozzle.

SI5.Electrical conductivity of CNT-PDMS films

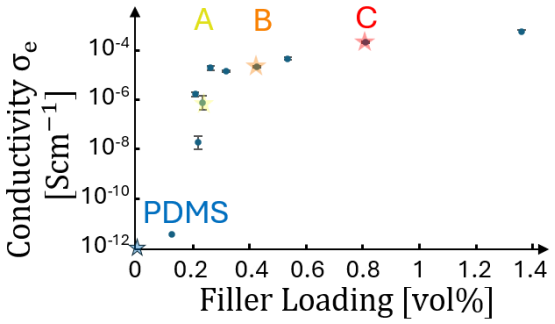

Figure S4. Electrical conductivity of CNT-PDMS composites as a function of filler loading, showing a percolation transition around 0.2 vol%.

SI6. Analytical model development

The framework establishes sensor design through the progression of:

SI6.1 - Construct constitutive curves of constituent cell materials

SI6.2 - Propagate constituent cell behavior to network response

SI6.3 - Evaluate network response and performance screening

SI6.1. Construct constitutive curves of constituent cell materials

For each constituent material, multiple samples were measured experimentally (SI6.1.1), their data was then combined to construct the constitutive $\sigma(\varepsilon)$ and $R(\varepsilon)$ curves (SI6.1.2).

SI6.1.1. Experimental measurement

Mechanical. Uniaxial tensile testing was performed according to ASTM D638 (Instron 5943, strain rate 0.5 % s^{-1}, air-pressure-controlled grips at 2 atm).

Electrical. Resistance was recorded in a four-wire configuration (Keysight B2961B, 10 µA). Gold-sputtered contacts were covered with liquid metal (Galinstan) to ensure low-impedance connection to the copper electrodes embedded in the tensile clamps, as shown in Figure S5.

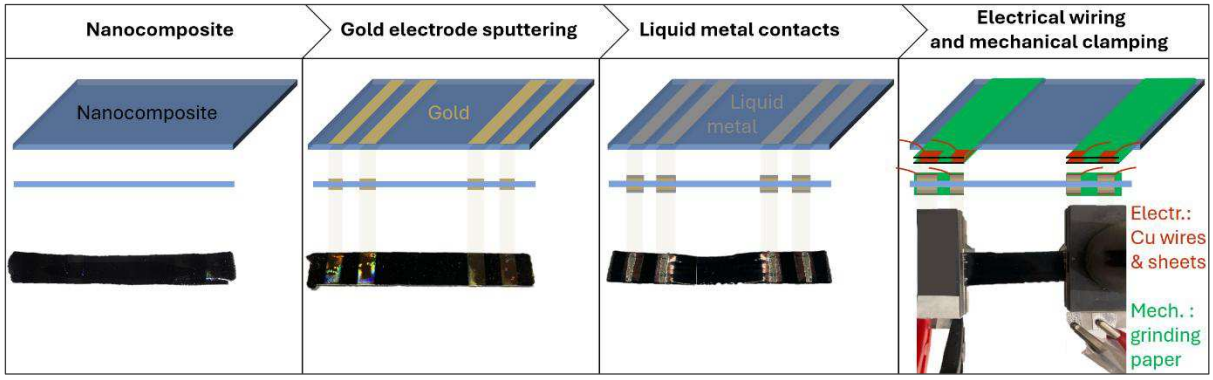

Figure S5 Fabrication and electrical interfacing of samples for electromechanical testing.

Electromechanical. Mechanical and electrical signals were recorded during tensile testing, and triggered simultaneously for a common time reference, as shown in Figure S6A. The electrical data $(t_e, R(t_e))$ was synchronized to the mechanical data $(t_m, \varepsilon(t_m), \sigma(t_m))$ by interpolation: $R(t_m) = \text{interp}(t_e, R(t_e), t_m)$, obtaining the $\sigma(\varepsilon)$ and $R(\varepsilon)$ curves (Figure S6B).

Dimensions. Optical microscopy accurately measured sample length and width. Thickness was calculated as $t = \frac{Volume}{Surface\ Area} = \frac{mass/density}{length*width}$. Mass was measured on a microbalance, and density via the Archimedes method. The gauge length was determined from the toe region of the $\sigma(\varepsilon)$ curve, corresponding to the clamp separation where the sample becomes taut.

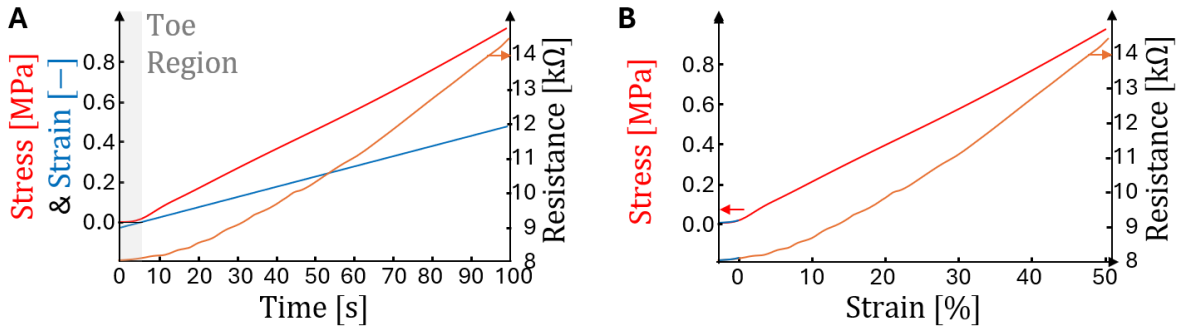

Figure S6. **(A)** Time synchronization of mechanical and electrical data (the toe region related to the initial sample slack was discarded). **(B)** The resulting $\sigma(\varepsilon)$ and $R(\varepsilon)$ curves of a sample.

SI6.1.2.Construct constitutive curves

For each constituent material, the constitutive $R(\varepsilon)$ curve was reconstructed from the $R(\varepsilon)$ curves of its samples. Simple averaging (mean or log-mean of R) was not suitable due to large sample-to-sample variation in baseline resistance R_0 (unstrained): When individual samples failed at a certain strain, severe vertical shifts of the mean occurred, distorting the group behavior into a stepwise shape as shown in Figure S7(red). To resolve this, the shape and baseline R_0 of the $R(\varepsilon)$ curve were reconstructed independently, using a derivative-integration method (related to elastic functional data analysis – EFDA[28]) in log-space, $r = \log R$:

i) Shape. Each sample's curve $r_i(\varepsilon)$ is differentiated to find the sample slope $s_i(\varepsilon)$, cancelling baseline R_0 offsets[19]. The constitutive slope is the average sample slope: $\bar{s}(\varepsilon) = \mathrm{AVG}[s_i(\varepsilon)]$. The constitutive curve is reconstructed by integration: $\bar{r}(\varepsilon) = \int \bar{s}(\varepsilon)\, d\varepsilon + cte$.

ii) Baseline r_0. The integration constant *cte* defines the baseline resistance of the $R(\varepsilon)$ curve. It is the average baseline r_0 of the unstrained samples: $cte = \mathrm{AVG}[r_i(\varepsilon = 0)]$.

The constitutive curve in Figure S7(green) has a representative shape for the samples over a large strain range. The mechanical response $\sigma(\varepsilon)$ was treated analogously. Confidence bands were estimated using bootstrap resampling. For a set of N samples, 300 resamples of size N were generated with replacement, and reconstructed. The 95% confidence band was defined by the 2.5th and 97.5th percentiles across these 300 reconstructions.

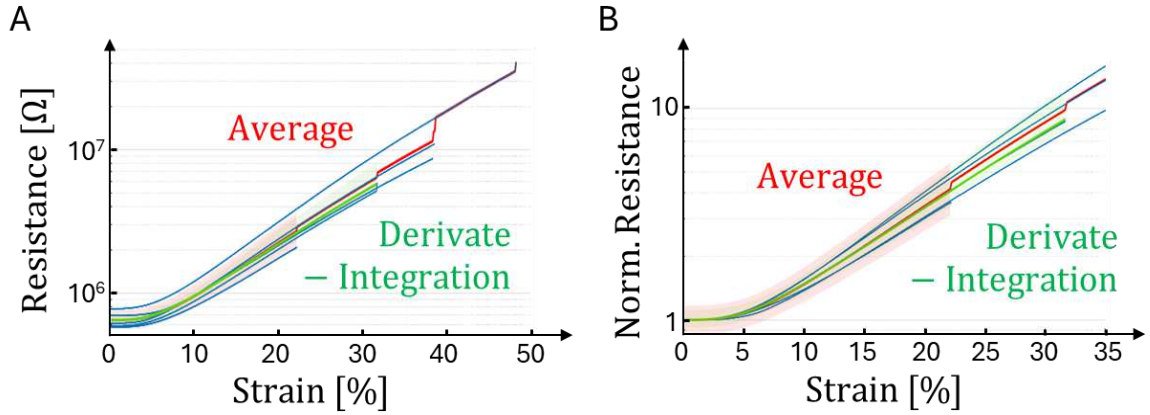

Figure S7. (A) Extraction of a constitutive $R(\varepsilon)$ curve from a set of samples (blue lines). Simple averaging (red curve) is distorted by baseline R_0 differences, while the derivative-integration method (green curve) yields a consistent curve over a wide strain range. Shaded area for 95% confidence bands.

To efficiently implement the analytical model, the reconstructed constitutive curves for $\sigma(\varepsilon)$ and $\log R(\varepsilon)$ were approximated by 3rd-order polynomials (all with R^2 above 0.99). $\sigma(\varepsilon)$ was constrained to pass through the origin, reflecting zero stress at zero strain. These closed-form Polynomials provide the constitutive curves as direct inputs to the analytical model (SI6.2).

SI6.2. Propagate constituent cell behavior to network response

SI6.2.1. Computation of model prediction

The metamaterial is modeled as a hierarchical resistor network with three levels:

Network. A network consists of branches in parallel. Given the resistance of each branch at the imposed strain $R_{\text{branch},j}(\varepsilon_{\text{branch}})$, the network resistance follows the parallel rule,

$$\frac{1}{R_{network}(\varepsilon_{global})} = \sum_j \frac{w_j}{R_{branch,j}(\varepsilon_{branch})} \quad \text{(Eq. S11)}$$

where w_j is the number of branches of type j in the network. Branches directly experience the imposed global strain (iso-strain condition), $\varepsilon_{\text{branch}} = \varepsilon_{\text{global}}$.

Branch. A branch consists of cells in series. Given the resistance of every cell $R_{\text{cell},i}(\varepsilon_{\text{cell},i})$, the branch resistance follows the series rule,

$$R_{branch}(\varepsilon_{global}) = \sum_i v_i R_{cell,i}\,(\varepsilon_{cell,i}) \quad \text{(Eq. S12)}$$

where v_i is the number of cells of constituent material i (e.g. A, B and C) in the branch.

Cell. The cell resistance $R_{\text{cell},i} = R_i(\varepsilon_{\text{cell},i})$ is extracted experimentally for each constitutive material and fitted analytically by a third order polynomial (section SI6.1). Thus, the problem reduces to determining the cell strain $\varepsilon_{\text{cell},i}$. Each material's constitutive stress-strain $\sigma_i(\varepsilon)$ fitted polynomial is analytically inverted using Cardano's method, giving $\varepsilon_i(\sigma)$. All cells in a branch share the same stress (iso-stress condition): $\sigma_{cell} = \sigma_{branch}$. The cell strain is

$$\varepsilon_{cell,i} = \varepsilon_i(\sigma_{branch}) \quad \text{(Eq. S13)}$$

Now that the cell strain $\varepsilon_{\text{cell},i}$ is expressed as a function of a branch stress, the model simply calculates the corresponding branch strain $\varepsilon_{\text{branch}}$ $(= \varepsilon_{\text{global}})$ and branch resistance R_{branch} over a σ_{branch} grid as follows:

- $\varepsilon_{\text{branch}}(= \varepsilon_{\text{global}})$ is the average of the cell material strains,

$$\varepsilon_{global}(\sigma_{branch}) = \varepsilon_{branch}(\sigma_{branch}) = \frac{1}{n_{cells}} \sum_i v_i \varepsilon_i(\sigma_{branch}) \quad \text{(Eq. S14)}$$

- R_{branch} is the sum of the cell material resistances,

$$R_{branch}(\sigma_{branch}) = \sum_i v_i\, R_i(\sigma_{branch}) = \sum_i v_i\, R_i[\varepsilon_i(\sigma_{branch}] \quad \text{(Eq. S15)}$$

This process yields a branch-specific table of $(\sigma_{\text{branch}}, \varepsilon_{\text{global}}, R_{\text{branch}})$ triplets, from which each actual $R_{\text{branch}}(\varepsilon_{\text{global}})$ value can be evaluated by interpolation. The calculated $R_{\text{branch}}(\varepsilon_{\text{global}})$ curves are shown as the solid lines in Figure S10, along with the experimental data (dashed lines with 95% confidence bands). This protocol replaces the need of solving a nonlinear system for every branch and strain point. Finally, by plugging the interpolated $R_{\text{branch}}(\varepsilon_{\text{global}})$ in Eq. S11, $R_{\text{network}}(\varepsilon_{\text{global}})$ is calculated.

SI6.2.2. Mechanical validation – Branch and Cell Strain

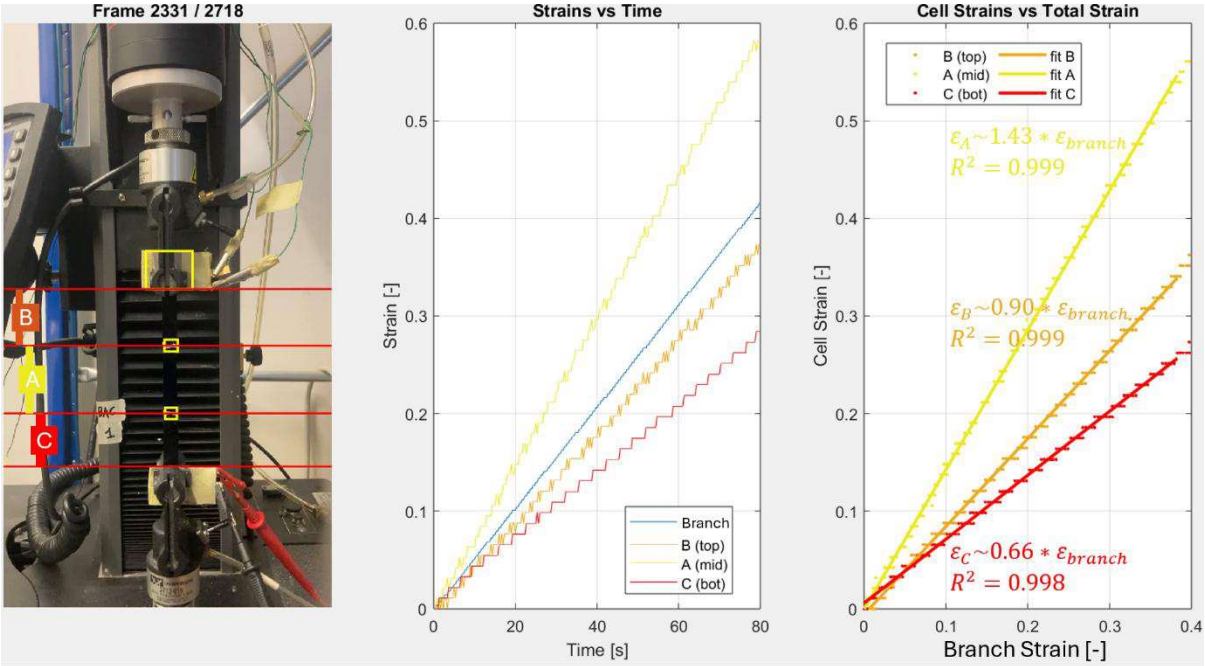

Figure S*8*. Image-based cell strain measurement, where cell lengths are tracked during tensile testing. Each cells relative strain is estimated as the slope of the $\varepsilon_{cell} - \varepsilon_{branch}$ curve via linear regression.

Figure S8 and video SI1 show how local cell strains were measured during tensile testing. Three thin reference marker lines were applied at the cell transitions, and their vertical positions were tracked in every frame using rigid 2D normalized cross-correlation. For each frame, the distances between the top clamp, internal white markers, and bottom clamp were measured to determine the cell lengths. Engineering strains were computed as $\varepsilon_i = \frac{L_i - L_{i,0}}{L_{i,0}}$ ($L_{i,0}$ is the initial length from the first frame) and plotted against the global strain. The relative cell strain was obtained as the slope of the linear regression of ε_i versus $\varepsilon_{\text{global}}$.

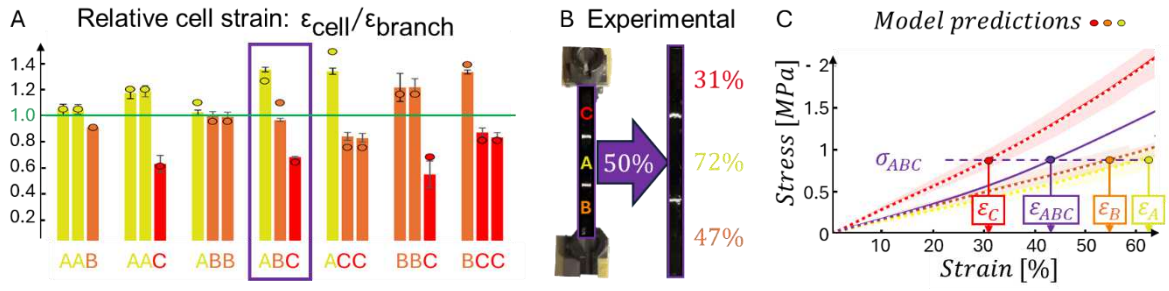

Figure S9. Strain redistribution in three-cell branches. **(A)** Relative cell strain for all branch types fabricated. The bars indicate experimental values and the circles predicted values. **(B)** Picture showing the experimental observation of local cell strains obtained via image-based strain tracking during tensile testing. **(C)** Model-predicted local cell strains based on the iso-stress condition.

SI6.2.3. Electrical validation – Branch resistance

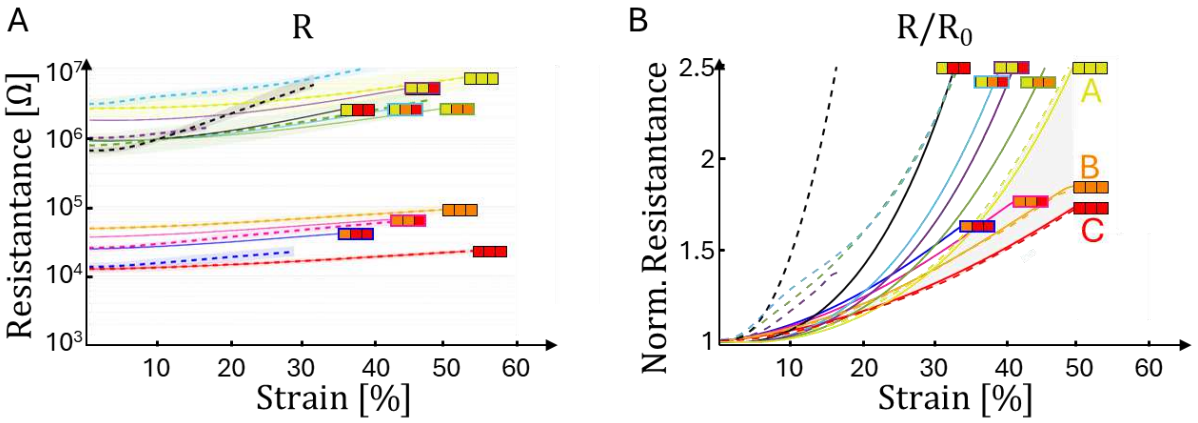

Figure S10 Electromechanical response of all branch types: (normalized) resistance versus strain. The model predictions (solid lines) are compared to experimental curves (dashed lines with shaded area for 95% confidence interval), reconstructed by the derivative-integration method in SI6.1. The branch configuration is indicated by the three constituent cells (A: yellow, B: orange, C: red). The curves with three equally-colored cells represent the homogeneous constituent materials.

SI6.2.4. Combinatorial design space and computational cost

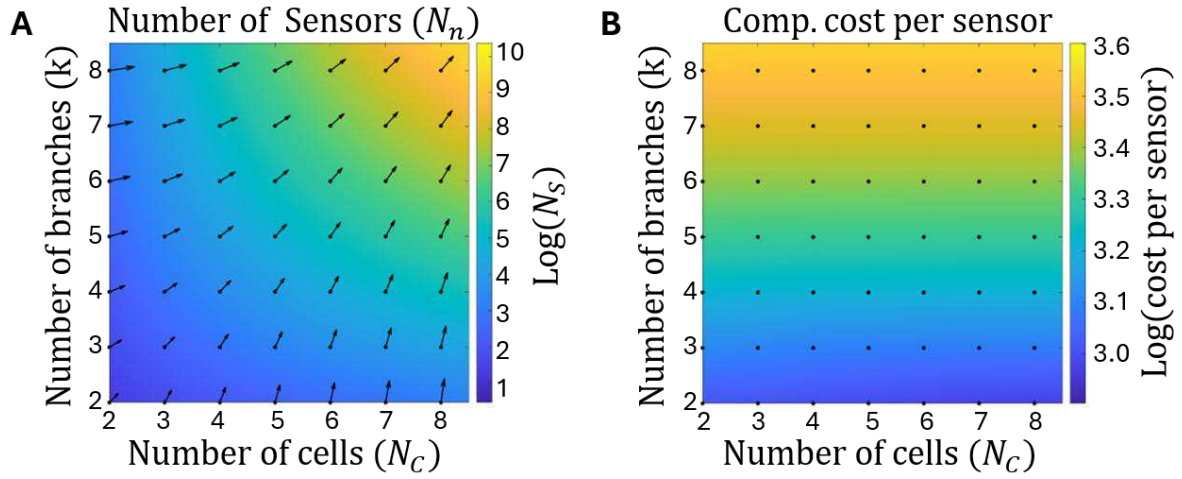

Figure S11. **(A)** combinatorial growth of the number of network architectures N_n and **(B)** the computational cost per predicted network, as functions of the number of cells N_C and branches k (for a fixed number of constituent materials N_m of 3). The gradient arrows in panel A point out the relative importance of including one more branch (y-axis) or cell (x-axis) for increasing the number of networks. The rapid growth of the design space highlights the impracticality of exhaustive experimental screening and motivates the use of the analytical physics-guided framework for inverse design.

Cells in series share identical stress, and branches in parallel share identical strain. Only the amount of each material in a branch and of each branch in a network matter, not their ordering. The number of branch/network configurations follows combinations-with-repetition counting. For branches composed of N_c cells drawn from N_m constituent materials, the number of distinct branch configurations is $N_b = \binom{N_c+N_m-1}{N_c}$. For networks composed of k branches drawn from N_b branch types, the number of distinct networks is $N_n = \binom{k+N_b-1}{k}$. These expressions grow combinatorially with both N_c and k. Even for moderate values, the configuration space becomes extremely large (e.g., reaching 53 thousand unique networks for only five cells per branch and five branches per network), as demonstrated in Figure S11A. Such spaces are impractical to explore experimentally, motivating analytical prediction of the relation between architecture and global sensor behavior. Crucially, since the architecture-to-response mapping is fully analytical, predicting without additional fitting or experimental work, so the problem shifts from prediction feasibility to computational efficiency.

The computational cost is separated into two stages:

Branch prediction cost. This stage resolves the nonlinear strain redistribution in branches. For each branch type (N_B), the model evaluates strain redistribution across N_C cells over a grid of S stress datapoints. Here, each cell's $\sigma(\varepsilon)$ and $R(\varepsilon)$ constitutive relations are discretized for selected stress points to find cell strain and cell resistance. These cell values are combined to obtain discrete values of branch strain and branch resistance, which are mapped onto a common strain grid via interpolation to construct a branch library: $R_{\text{branch,i}}(\varepsilon_{global})$. Operations scale linearly with the number of cells N_C and stress points S, giving a per-branch and total cost of:

$$T_{branch,i} = O(N_C S); \qquad T_{branches} = N_B * T_{branch,i} = O(N_B N_C S) \qquad \text{(Eq. S16)}$$

Network prediction cost. The network response is obtained by combining k branch resistances in parallel. Operations scale linearly with both k and S, giving a per-network and total cost of:

$$T_{network,i} = O(kS); \qquad T_{networks} = N_N * T_{network,i} = O(N_N kS). \qquad \text{(Eq. S17)}$$

The total computational cost scales as:

$$T_{\text{total}} = T_{\text{branches}} + \mathrm{T}_{\text{networks}} = O(N_B N_C S) + O(N_N kS). \qquad \text{(Eq. S18)}$$

The exploration efficiency —i.e., the cost per evaluated network— is shown in Figure S11B:

$$\frac{T_{\text{total}}}{N_N} = O\left(\frac{N_B N_C S}{N_N}\right) + O(kS). \qquad \text{(Eq. S19)}$$

The first term represents the branch-library overhead, scaling only linearly with N_B and N_C. In contrast, the number of networks N_N grows combinatorially with both N_B and k. For metamaterial designs ($k \geq 2$), this combinatorial growth ensures that N_N is much larger than $N_B N_C$. Consequently, the branch-library overhead becomes rapidly amortized when computing the cost per candidate network, and the per-network cost approaches $O(kS)$. Increasing k raises the number of networks but also increases the per-candidate cost roughly linearly. In contrast, increasing N_C expands the design space combinatorially while adding only limited evaluation cost. Importantly, increasing N_C enhances the nonlinear strain-redistribution within branches rather than the less interesting averaging effect produced by larger k. As a result, increasing N_C is a particularly efficient exploration strategy: it yields a much richer set of electromechanical behaviors at nearly the same per-network computational cost.

SI6.3. Evaluate network response and performance screening

The key metrics are linearity (R^2), sensitivity (*GF*) and linear strain range. For every strain ε_{end}, regression over the interval $[0, \varepsilon_{end}]$ yields three interdependent metrics: (1) R^2, the linearity. (2) GF_{fit}, the regression slope. (3) ε_{end}, the strain range. Thus, a sensor does not possess a single *GF* or R^2; instead, it traces a trajectory in the (ε_{end}, GF_{fit}, R^2) space, shown in Figure S12A.

Reported strain range and gauge factor in manuscript Figure 3(E,F). To compare sensor performance, the 3D trajectory was reduced to a single representative point per sensor. This required a consistent rule for selecting a meaningful combination of (ε_{end}, GF_{fit}, R^2). Because linearity is essential for practical sensing, a minimum linearity (e.g., $R^2 \geq 0.98$, green region in Figure S12B) was imposed to find the strain range that behaves sufficiently linearly. The corresponding ε_{end} defines the linear strain range, where *GF* is the slope of that regression.

Interdependent metrics. Because linearity, sensitivity, and strain range are interdependent, sensor performance should be evaluated in the 3D space rather than through a single metric. Each sensor's trajectory in (ε_{end}, GF_{fit}, R^2) allows performance selection by a 3D plane-sweep:
1) If linearity is the only limitation, we draw a perpendicular plane to the R^2 direction (normal vector $\vec{n} = (0,0,1)$) and place it at the desired R^2 point. All points below the plane have insufficient linearity and are eliminated.
2) If sensitivity is the only limitation, the protocol above must be followed but with a plane whose normal vector is the GF_{fit} direction $\vec{n} = (0,1,0)$.
3) If strain range is the only limitation, the protocol above must be followed but with a plane whose normal vector the ε_{end} direction $\vec{n} = (1,0,0)$.
4) In general, the three metrics matter. We assign weights to the relative importance of each to define a normal vector $\vec{n} = (w_\varepsilon, w_{GF}, w_{R^2})$. Sweeping a perpendicular plane along $\vec{n}$ identifies the points – and sensors – furthest along this direction, representing optimal performance. Figure S12A shows an example sweep for $(w_\varepsilon, w_{GF}, w_{R^2}) = (1,0.1,1)$. The plane-sweep procedure is equivalent to projecting each point (ε_{end}, GF_{fit}, R^2) onto $\vec{n}$ and ranking them by the projection score: (ε_{end}, GF_{fit}, R^2) $* \vec{n}$, where the score signifies combined performance. This geometric viewpoint naturally handles the interdependence of the three metrics, which is highly valuable because it enables multi-objective optimization.

The network response is computed analytically and deterministically, enabling pre-selection of promising sensor candidates prior for fabrication, rather than experimental iteration over sensor prototypes, and rational narrowing of the design space.

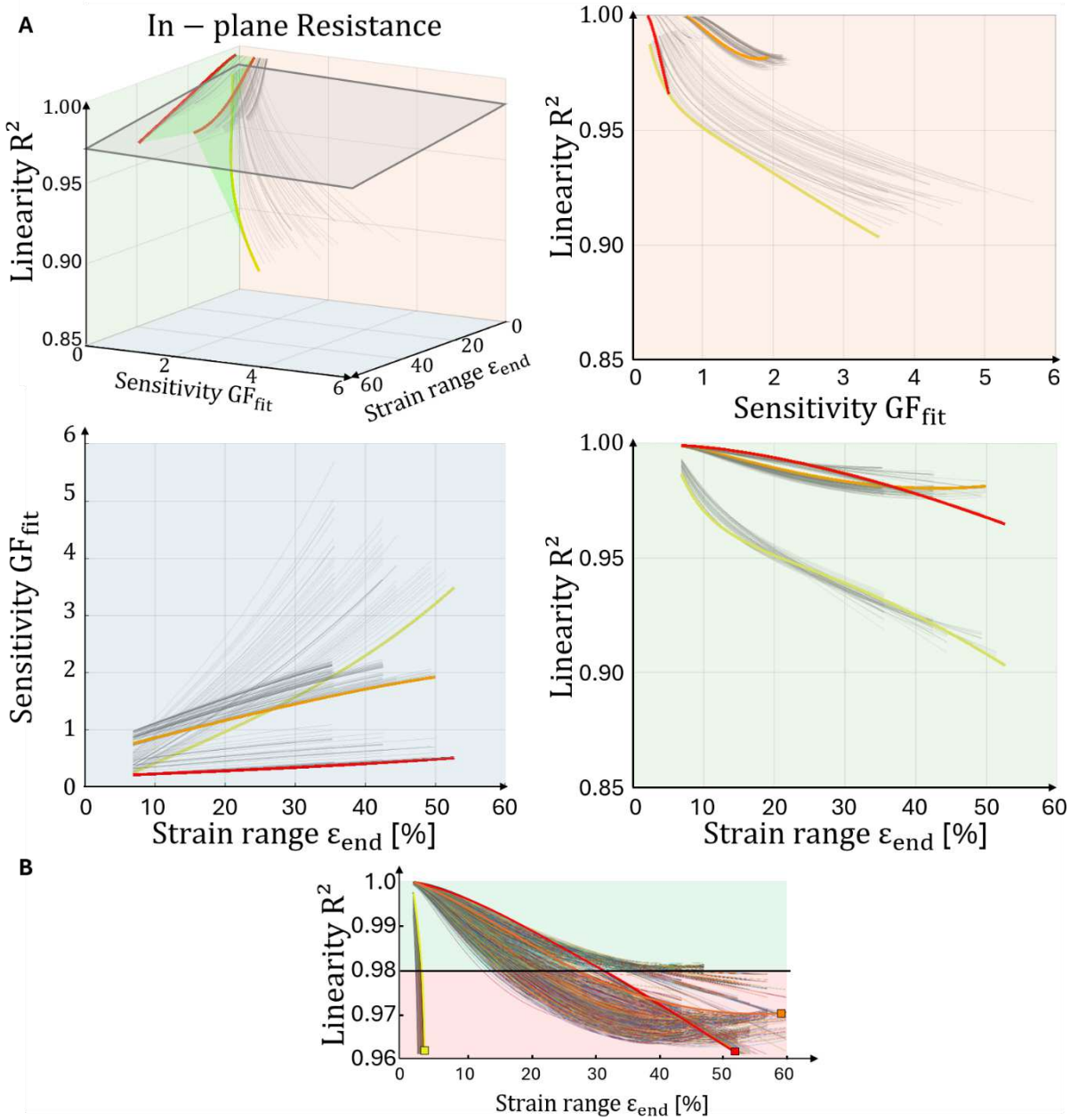

Figure S12 In-plane resistance sensing, with performance metrics extracted from the predicted $R(\varepsilon)$. (A) Each sensor produces a 3D trajectory in (ε_{end}, GF_{fit}, R^2) space, enabling multi-objective optimization of the 3 interdependent metrics. To visualize their position in 3D, projections onto the three principal planes (blue, red, green) are added. These also demonstrate how the meta gauges escape the envelope of their constituent materials (green planes connecting constituent material trajectories), most notably in the $\varepsilon_{\text{end}} - GF_{\text{fit}}$ (blue) plane. (B) Linearity-based selection for the data reported in Figure 3. Each sensor's trajectory in (ε_{end}, GF_{fit}, R^2) space is visualized in 3D, along with projections onto the three principal planes (blue, red, green).

SI7. Alternative sensing modes of metamaterials

			Branch	Network 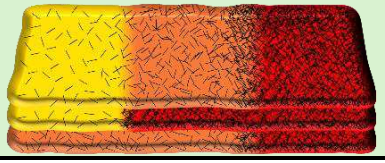
Mechanical	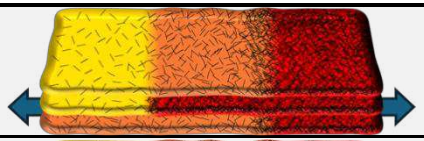	**In-Plane** Tensile Strain	Parallel (Iso-Stress, Reuss) $E_{branch}^{-1} = \sum E_{cell}^{-1}$	Series (Iso-Strain, Voight) $E_{netw} = \sum E_{branch}/k$
	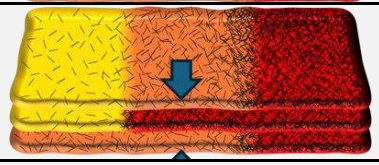	**Through-Plane** Compr. stress	Series (Iso-Strain, Voight) $E_{branch} = \sum E_{cell}/k$	Parallel (Iso-Stress, Reuss) $E_{netw}^{-1} = \sum E_{branch}^{-1}$
Functional	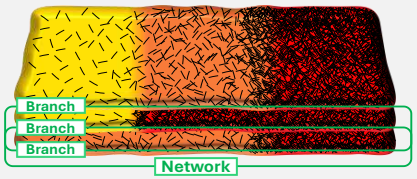	**In-plane** Resistance	Series $R_{branch} = \sum R_{cell}$	Parallel $R_{netw}^{-1} = \sum R_{branch}^{-1}$
		In-plane Capacitance	Parallel $C_{branch}^{-1} = \sum C_{cell}^{-1}$	Series $C_{netw} = \sum C_{branch}$
	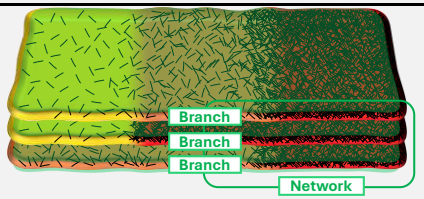	**Through-plane** Resistance	Parallel $R_{branch}^{-1} = \sum R_{cell}^{-1}$	Series $R_{netw} = \sum R_{branch}$
		Through-plane Capacitance	Series $C_{branch} = \sum C_{cell}$	Parallel $C_{netw}^{-1} = \sum C_{branch}^{-1}$

Table S2. Overview of metamaterial architectures for sensing modes and corresponding physical laws.
These systems combine mechanical (in-plane strain or through-plane compression) and functional loading (in-plane or through-plane, resistance R or capacitance C). k is the number of branches. For piezoelectric materials, in-plane voltage would show behavior similar to in-plane R (branch series and network parallel). Non-traditional behavior can be attained with these architectures.

The sensitivity or gauge factor is now in fact a transverse gauge factor, where the electrical response is measured in one direction while the mechanical strain is applied in another. Similar to in-plane resistance sensing, the metamaterials exhibit unconventional behavior in through-plane sensing for both resistance (Figure S13) and capacitance (Figure S14). This is evident as the metamaterial designs (grey lines) fall outside the envelope between the three starting materials, represented as green planes in the 3D visualization.

However, unlike in-plane resistance sensing - where metamaterials displayed higher sensitivity and/or linearity (blue and red projections in Figure S12) - through-plane sensing shows a consistent trade-off: higher linearity comes at the expense of lower sensitivity (red projections in Figure S13 and Figure S14) This trade-off arises from the fundamental physical laws: Through-plane sensing is dominated by the cell with the lowest resistance $R_{branch}^{-1} = \sum R_{cell}^{-1}$ and highest capacitance ($C_{branch} = \sum C_{cell}$), which corresponds to the C material. In contrast to in-plane resistance, where the electrically dominant A material (the softest) experiences strain amplification to boost sensitivity, the electrically dominant C material (the stiffest) in through-plane sensing undergoes strain reduction, reducing sensitivity.

Through-plane sensing demonstrates superior linearity ($R^2 > 0.98$ for most designs) when compared to in-plane sensing ($R^2 > 0.96$ for most designs, though some highly sensitive A material-based designs dip to $R^2 > 0.9$). Although all sensors maintain extreme linearity ($R^2 > 0.98$) across a broad strain range, through-plane sensing exhibits markedly lower sensitivity. Its maximum *GF* reaches around 1.2 for capacitance and -0.5 for resistance at the maximum strain range ε_{end}, compared to the *GF* of 3-5 achieved by in-plane resistance sensing. Importantly, the objective is not universally to maximize sensitivity; different applications may instead prioritize response stability, extreme linearity, or reduced electromechanical coupling. For example, the through-plane capacitance sensing mode has a range of metamaterials that have lower sensitivity and higher linearity than the constituent materials, making them more suitable for strain-invariant stretchable electronics such as amplifiers and transistors.

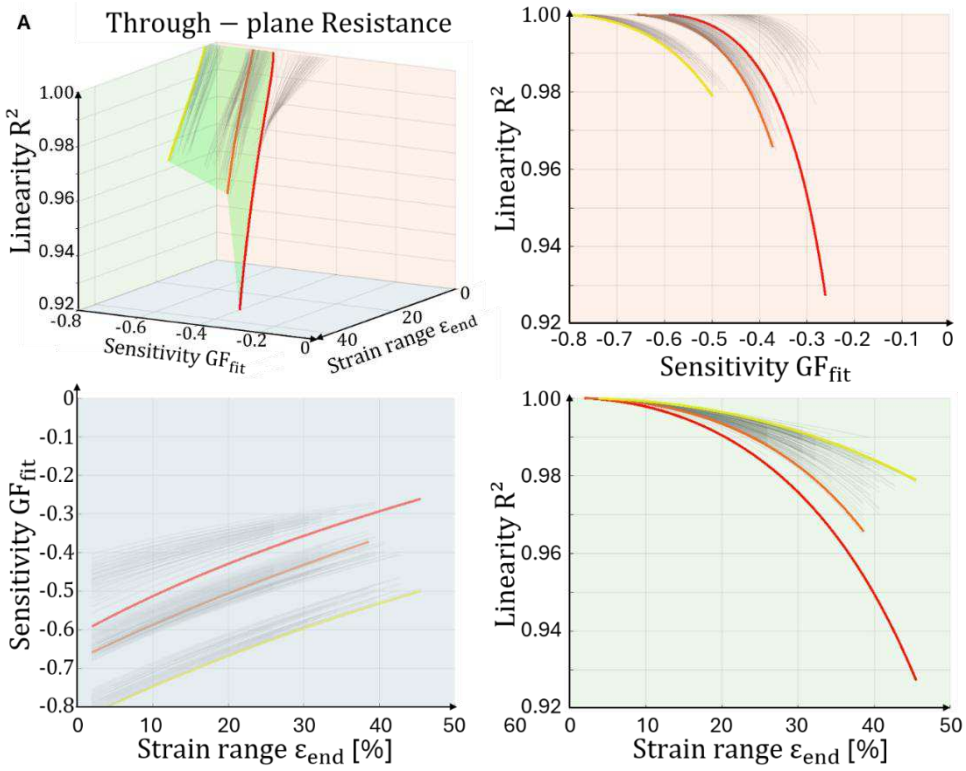

Figure S13 Through-plane resistance sensing. Each sensor's trajectory in $(\varepsilon_{\text{end}}, GF_{\text{fit}}, R^2)$ space is visualized in 3D, along with projections onto the three principal planes (blue, red, green). The sensitivity or gauge factor is now in fact, a transverse gauge factor, where the electrical response is measured in one direction while the mechanical strain is applied in another.

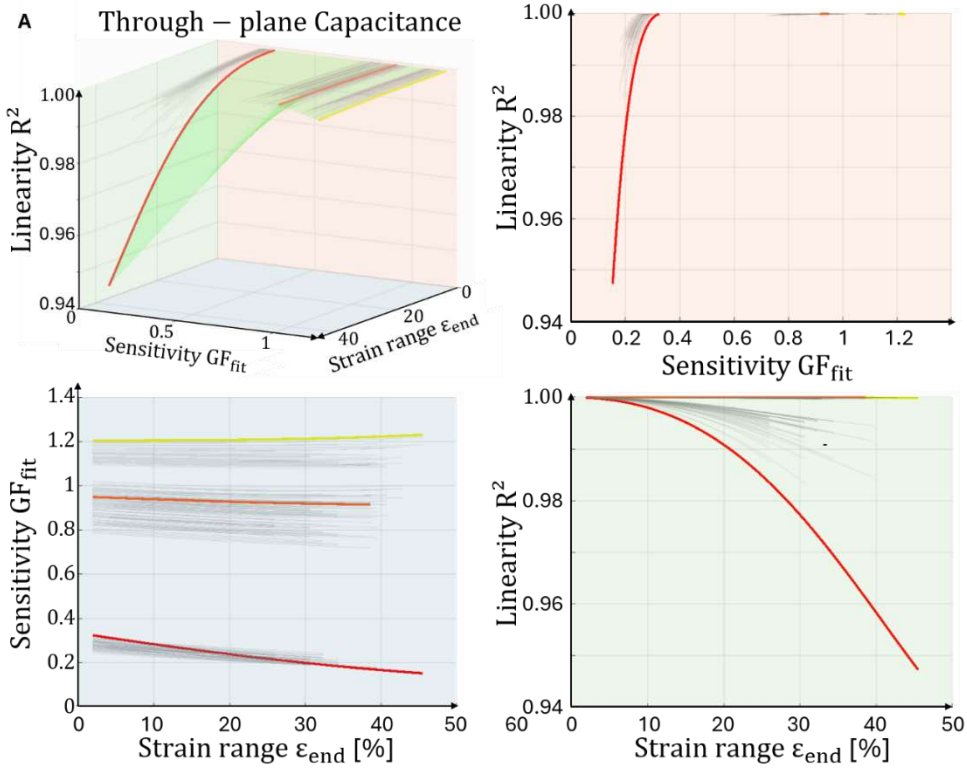

Figure S14 Through-plane capacitive sensing. Each sensor's trajectory in $(\varepsilon_{\text{end}}, GF_{\text{fit}}, R^2)$ space is visualized in 3D, along with projections onto the three principal planes (blue, red, green). The sensitivity or gauge factor is now, in fact, a transverse gauge factor, where the electrical response is measured in one direction while the mechanical strain is applied in another.

SI8. Application: Strain Tracking and Regression

Video SI2 illustrates how sensor strain was extracted by tracking the relative motion of the two clamp fixtures during breathing. For each video frame, the distance between the clamps was determined using a two-stage tracking procedure, applied to the stripe pattern on each clamp. First, a course update on the pattern positions by applying 2D normalized cross-correlation, with the stripe pattern as template. Second, the pattern position and orientation are refined using the known geometric ratios of black-white stripes (Thales theorem). From the exact pattern positions, the clamp-to-clamp distance (in pixel units) is computed. A conversion factor (mm/px) is computed using the real dimensions of the printed pattern, to obtain the real clamp-to-clamp distance [mm].. Engineering strain is computed as $\varepsilon_i = \frac{L_i - L_0}{L_0}$, where L_0 is the minimum observed length (where the strap and sensor are not slack).

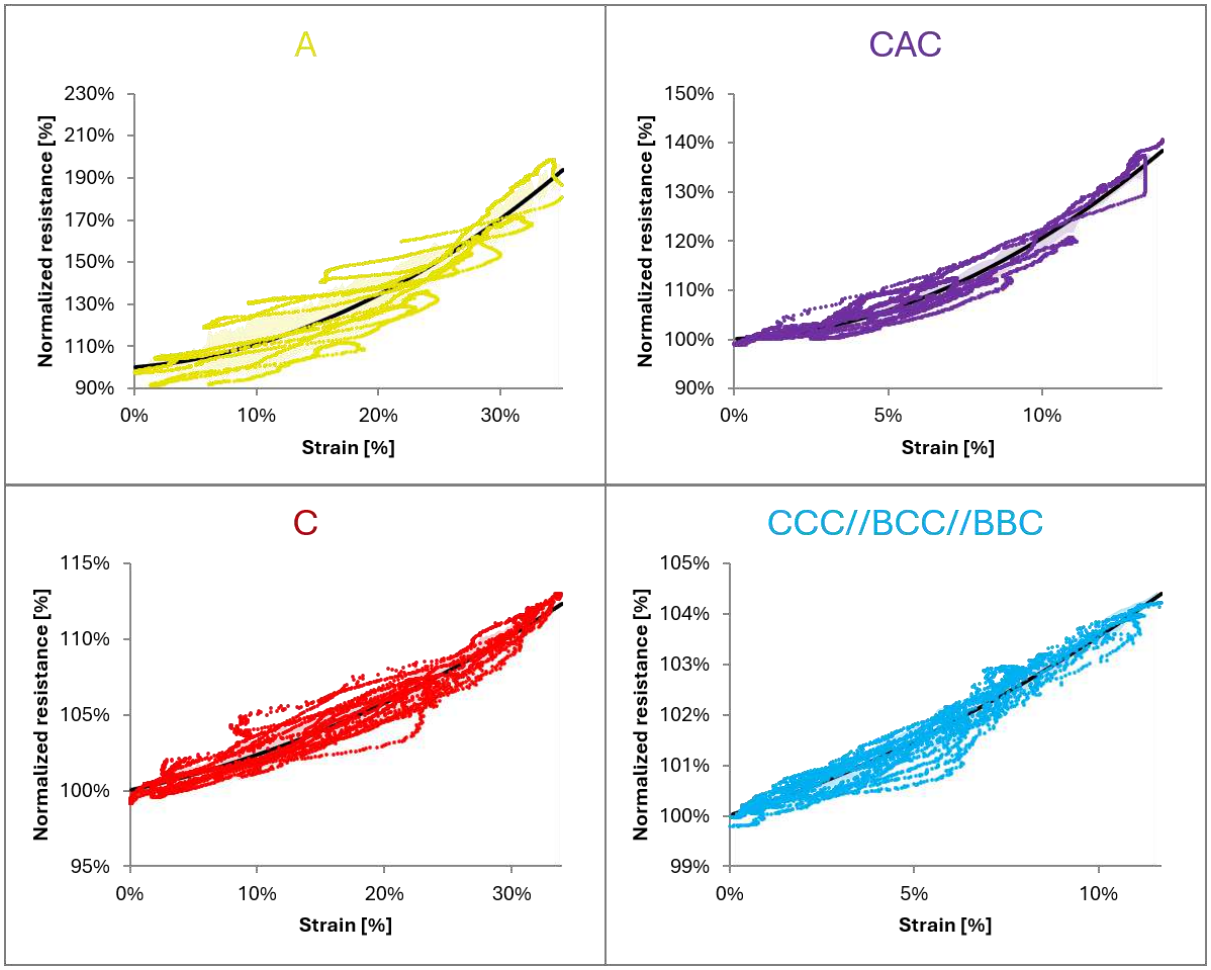

Figure S15 Regression of normalized resistance vs strain, for the four measured sensors.

The regression curves and 95% prediction intervals presented in Figure 4C were calculated from the raw dataset of (strain, resistance) Vs. time, shown in Figure 4B. The 2nd order polynomials were only used to illustrate concisely the general behavior, i.e. the sensitivity (average slope) and linearity (curvature) of the sensors. The intercept (b_0) was set to 1 to impose that $R=R_0$ for the unstrained sensors.

References – supporting information

1. Du, J. et al. Optimized CNT-PDMS Flexible Composite for Attachable Health-Care Device. *Sensors* **20**, 4523 (2020).
2. Cui, X. et al. Sensing performance and mechanism of flexible sensing-enabled CB-CNT/PDMS geosynthetics for soil deformation monitoring. *Geotext. Geomembr.* **54**, 348–361 (2026).
3. Liu, L. et al. Highly stretchable, sensitive and wide linear responsive fabric-based strain sensors with a self-segregated carbon nanotube (CNT)/Polydimethylsiloxane (PDMS) coating. *Prog. Nat. Sci.: Mater. Int.* **32**, 34–42 (2022).
4. Amjadi, M. & Park, I. Carbon nanotubes–Ecoflex nanocomposite for strain sensing with ultra-high stretchability. In *2015 28th IEEE International Conference on Micro Electro Mechanical Systems (MEMS)* 744–747 (IEEE, 2015).
5. Ryu, S. et al. Extremely Elastic Wearable Carbon Nanotube Fiber Strain Sensor for Monitoring of Human Motion. *ACS Nano* **9**, 5929–5936 (2015).
6. Zhang, Q. et al. Highly Sensitive and Stretchable Strain Sensor Based on Ag@CNTs. *Nanomaterials* **7**, 424 (2017).
7. Nankali, M. et al. Highly stretchable and sensitive strain sensors based on carbon nanotube–elastomer nanocomposites: the effect of environmental factors on strain sensing performance. *J. Mater. Chem. C* **8**, 6185–6195 (2020).
8. Wang, Y. et al. Fabrication of high-performance wearable strain sensors by using CNTs-coated electrospun polyurethane nanofibers. *J. Mater. Sci.* **55**, 12592–12606 (2020).
9. Huang, A. et al. Durable washable wearable antibacterial thermoplastic polyurethane/carbon nanotube@silver nanoparticles electrospun membrane strain sensors by multi-conductive network. *Adv. Compos. Hybrid Mater.* **6**, 101 (2023).
10. Dou, L. et al. Weft-Knitted Spacer Fabric for Highly Stretchable–Compressible Strain Sensor, Supercapacitor, and Joule Heater. *Nanomaterials* **12**, 3684 (2022).
11. Wang, Y. et al. Fabrication of ultra-high working range strain sensor using carboxyl CNTs coated electrospun TPU assisted with dopamine. *Appl. Surf. Sci.* **566**, 150705 (2021).
12. Wang, X., Qu, M., Wu, K., Schubert, D. W. & Liu, X. High sensitive electrospun thermoplastic polyurethane/carbon nanotubes strain sensor fitting by a novel optimization empirical model. *Adv. Compos. Hybrid Mater.* **6**, 63 (2023).
13. Zhou, B. et al. A Highly Sensitive and Flexible Strain Sensor Based on Dopamine-Modified Electrospun Styrene-Ethylene-Butylene-Styrene Block Copolymer Yarns and Multi Walled Carbon Nanotubes. *Polymers* **14**, 3030 (2022).
14. Nemala, S. S. et al. Electrically Conductive Nanocarbon/Elastomer Composite Inks for Flexible and Wearable Strain Sensing. *Small* **21**, e06844 (2025).
15. Jia, B. et al. Flexible strain sensors based on carbon nanotubes/polydimethylsiloxane composites with a segregated structure prepared by sustainable emulsion method. *Polym. Eng. Sci.* **65**, 1093–1105 (2025).
16. Mai, H., Mutlu, R., Tawk, C., Alici, G. & Sencadas, V. Ultra-stretchable MWCNT–Ecoflex piezoresistive sensors for human motion detection applications. *Compos. Sci. Technol.* **173**, 118–124 (2019).
17. Li, Y. et al. Continuously prepared highly conductive and stretchable SWNT/MWNT synergistically composited electrospun thermoplastic polyurethane yarns for wearable sensing. *J. Mater. Chem. C* **6**, 2258–2269 (2018).

18. Amjadi, M., Yoon, Y. J. & Park, I. Ultra-stretchable and skin-mountable strain sensors using carbon nanotubes–Ecoflex nanocomposites. *Nanotechnology* **26**, 375501 (2015).
19. Wang, G. et al. Thermoplastic Polyurethane/Carbon Nanotube Composites for Stretchable Flexible Pressure Sensors. *ACS Appl. Nano Mater.* **6**, 9865–9873 (2023).
20. Xu, Y. et al. Encapsulated core–sheath carbon nanotube–graphene/polyurethane composite fiber for highly stable, stretchable, and sensitive strain sensor. *J. Mater. Sci.* **56**, 2296–2310 (2021).
21. Guo, H. et al. Nacre-mimetic electronic skin based on multilayered Ti3C2Tx/carbon nanotubes/thermoplastic polyurethane fibrous mat with self-powered ability for postural correction training. *Sci. China Mater.* **68**, 4253–4262 (2025).
22. Chen, R. et al. Waterborne polyurethane toughened carbon nanotube paper with excellent Joule heating properties and strain-sensing potential. *Carbon Lett.* **35**, 2423–2434 (2025).
23. Yin, F., Ye, D., Zhu, C., Qiu, L. & Huang, Y. Stretchable, Highly Durable Ternary Nanocomposite Strain Sensor for Structural Health Monitoring of Flexible Aircraft. *Sensors* **17**, 2677 (2017).
24. Hou, Y., Zhang, H. & Zhou, K. Ultraflexible Sensor Development via 4D Printing: Enhanced Sensitivity to Strain, Temperature, and Magnetic Fields. *Adv. Sci.* **12**, 2411584 (2025).
25. Zhou, J., Xu, X. & Lubineau, G. Devices and methods relating to fragmented carbon nanotube sensors. US patent 11,073,385 (2021).

Supplementary Files

This is a list of supplementary files associated with this preprint. Click to download.

- SI1.docx
- VideoS2.mp4
- VideoS1.mp4